8-2012

Fabrication and Characterization of Thermomechanically Processed Sulfur and Boron Doped Amorphous Carbon Films

Lonnie Carlson
University of Nebraska-Lincoln, lonnie.carlson@gmail.com

FABRICATION AND CHARACTERIZATION OF THERMOMECHANICALLY PROCESSED SULFUR AND BORON DOPED AMORPHOUS CARBON FILMS

by

Lonnie Carlson

A DISSERTATION

Presented to the Faculty of

The Graduate College at the University of Nebraska

In Partial Fulfillment of Requirements

For the Degree of Doctor of Philosophy

Major: Engineering

(Materials Engineering)

Under the Supervision of Professor Jennifer I. Brand

Lincoln, Nebraska

August, 2012

FABRICATION AND CHARACTERIZATION OF THERMOMECHANICALLY PROCESSED SULFUR AND BORON DOPED AMORPHOUS CARBON FILMS

Lonnie Carlson, Ph.D.
University of Nebraska, 2012

Adviser: Jennifer I. Brand

Small scale, high power density, reliable, and long-life power supplies would be useful or even critical for space missions or the growing number of microdetectors, microsensors, and miniature vehicles. Alpha or beta particle voltaic devices could satisfy these requirements but have been shown to degrade quickly due to radiation damage. Amorphous carbon (a-C) PN junctions or PIN devices could provide radiation hardness and sufficiently high efficiency. As the range of alpha and beta particles in a-C is ~20-120μm, much thicker films than are typical are needed to maximize collection of the particle energy.

In this work, the fabrication of thermomechanically processed p- and n-type doped a-C films were investigated as a first step in the future development of radiation hard voltaic devices. Boron carbide (B_4C) powder was mixed with a-C nanopowders as a possible p-type dopant with sulfur powder utilized as a possible n-type dopant. Doping levels of 2.5at%, 5.0at%, and 10.0at% were investigated for both dopants with films pressed at 109°C over a pressure range of 0.3-5.0GPa. Initial attempts to fabricate rectifying PN junctions and PIN devices was unsuccessful.

Bonding properties were characterized using Raman spectroscopy with electronic properties primarily assessed using the van der Pauw method. Undoped a-C and boron-doped films were found to be slightly p-type with sulfur-doped films converting to n-type. All films were found to consist almost entirely of nano-graphitic sp^2 rings with only slight changes in disorder at different pressures. Sulfur doped films were less brittle which is indicative of crosslinking.

Boron doping did not significantly change the film electronic properties and is not an effective dopant at these temperatures and pressures. Sulfur doping had a greater effect and could likely be utilized as basis for an n-type material in a device. Initial irradiation studies using alpha particles showed that boron and undoped films became more p-type with sulfur films converting to p-type. The sulfur doped films returned to n-type after isothermal annealing.

Acknowledgements

First and foremost, I'd like to thank my wife Sherri and daughters Dani and Katie for your unequivocal support and understanding when I would sleep in my office for days at a time and only come home on the weekends. Couldn't have done this without you.

I would like also to express my sincere appreciation to Professor Jennifer Brand for her support throughout this process. Her patience and understanding as I seemingly scheduled my research around the various family medical issues that assaulted us the last two years was instrumental in me maintaining my sanity while successfully accomplishing the mission.

Special thanks to Prof. Ianno., Prof. Lu, and their grad students Ami, Wei, and Masoud for the access to, training on, and assistance with the Hall effect equipment and Raman Spectrometer.

I am also grateful to the other members of my dissertation committee: Profs. Susan Hallbeck, Paul Savory, and Gustavo Larsen. Your time, assistance, and feedback is much appreciated.

Table of Contents

Acknowledgements ..... **iv**

Table of Contents ..... **v**

List of Figures ..... **viii**

List of Tables ..... **xi**

1. Introduction **12**

1.1. Motivation **12**

1.2. Background **13**

1.3. Critical Properties For Effective Radioisotope Voltaics **16**

1.4. Problem Statement **19**

1.5. Research Methodology **19**

2. Amorphous Carbon Films **20**

2.1. Introduction **20**

2.1.1 Carbon Materials. 20

2.1.2 Carbon Doping. 26

2.1.3 Thermomechanical Processing. 27

2.2. Film Pressing Apparatus **28**

2.2.1 Precursor Materials. 28

2.2.2 Powder Mixing 29

2.2.3 Film Pressing 30

3. Film Growth Procedures **30**

3.1. Undoped Films **30**

3.2. Doped Film Growth 33

4. Amorphous Carbon Film Characterization 34

4.1. Raman Spectroscopy 34

4.1.1 Introduction 34

4.1.2 Apparatus and Procedure 38

4.1.3 Film Imaging 39

4.1.4 Carbon Nanopowder Raman Baseline 40

4.1.5 Thermomechanically Processed Undoped Carbon Raman Results 42

4.1.6 Sulfur Doped Film Raman Results 44

4.1.7 Boron Doped Film Raman Results 45

4.2. Resistivity Measurements 46

4.2.1 Introduction 46

4.2.2 Apparatus and Procedure 48

4.2.3 Results 49

4.2.4 Undoped Film Resistivity 49

4.2.5 Sulfur Doped Film Resistivity 50

4.2.6 Boron Doped Film Resistivity 53

4.3. Hall Effect Measurements 56

4.3.1 Introduction 56

4.3.2 Apparatus and Procedure 58

4.3.3 Hall Voltage Results 59

4.3.4 Carrier Concentration Results 61

4.3.5 Carrier Mobility Results 62

5. PN Junction/PIN Device Fabrication and Characterization 64

5.1. PN Junction and PIN Diodes Introduction 64

5.2. Thermomechanical PN Junction and PIN Diode Fabrication Apparatus and Procedure 66

5.3. Plasma Enhanced Chemical Vapor Deposition (PECVD) Apparatus 67

5.4. PECVD PN Junction and PIN Device Procedure 74

5.5. Characterization Apparatus and Procedure 76

5.6. PN Junction and PIN Device Results 77

5.6.1 Thermomechanically Processed PN Junction and PIN Devices 77

5.6.2 PECVD Processed PN Junction and PIN Devices 79

6. Effects of Radiation 82

6.1. Radiation Damage 82

6.2. Radiation Transport. 83

6.3. Apparatus and Procedure 84

6.4. Postirradiation Results 85

7. Conclusions 89

7.1. Undoped and Doped Carbon Films 89

7.2. PN Junction and PIN Devices 93

8. Recommendations for future research. 93

Appendix A van der Pauw Worksheet 100

Appendix B Wilcoxon Sign Test 101

Appendix C Detailed PECVD Procedure 102

List of Figures

Figure Page

Figure 2-1. Common allotropes of carbon. CNT are carbon nanotubes. [13] 21
Figure 2-2. sp^3, sp^2, sp^1 hybridized carbon bonding. sp^3 bonding, as in diamond, occurs when the four valence electrons bond tetrahedrally with adjacent atoms via σ bonds. sp^2 bonding, as in graphite, occurs when three valence electrons form σ bonds in the plane and one electron forms a π bond normal to the σ bond plane. sp^1 bonds occur when two valence electrons form σ bonds along the ± x axis while the other two electrons form π bonds along the y and z axis. [15] 22
Figure 2-3 Amorphous carbon ternary phase diagram. sp^2 corresponds to graphite, sp^3 to diamond, and H to hydrocarbons. GLCH and PLCH are graphite and polymer like hydrogenated carbons. [16] 23
Figure 2-4. Pressure-temperature diagram of carbon. This work will focus on the area below 600K and 5GPa. See reference for full description. [14] 24
Figure 2-5. sp^2 fraction vs. experimental optical gap for disordered carbons. The optimal gap for a voltaic cell is ~ 1eV. [15] 25
Figure 2-6. Cyclooctasulfur S_8 ring. [31] 28
Figure 2-7. Boron carbide (B_4C) nominal structure. [32] 29
Figure 2-8. Wig-L-Bug grinder/mixer. 29
Figure 2-9. PHI-Tulip heated/cooled programmable 30-ton hydraulic press. 30
Figure 3-1. 70mm stainless steel pusher plates used to protect press platen. 32
Figure 4-1. Schematic of inelastic scattering that is the basis of Raman spectroscopy. Unheated carbon measurements are in the Stokes scattering regime. [45] 35
Figure 4-2. Schematic of a Raman spectrometer. 35
Figure 4-3. Schematic of sp^2 bonding influences on 514nm Raman spectra of disordered carbons. [45] 36
Figure 4-4. Schematic variation of the I_D/I_G ratio and the G peak dispersion. [45] 37
Figure 4-5. Renishaw InVia Raman Spectrometer. The spectrometer has 514nm, 633nm, and 785nm lasers to cover a range of excitation energies. 38
Figure 4-6. Film images taken through the 5X and 100X Raman microscope objective lenses. 40
Figure 4-7. Baseline Raman spectra of a-C, graphitized carbon black (GCB), and nanodiamond powders using a 514nm laser. 41
Figure 4-8. 514nm Raman spectra raw data of thermomechanically pressed a-C showing no significant change in G peak position with pressure. 43
Figure 4-9. Raman data for pressed a-C films. G peak position generally decreases as pressure increases while I_D/I_G ratio generally increases with pressure. G peak dispersion is very low and implies the film is largely nano-graphitic. 44
Figure 4-10. Raman data for sulfur-doped pressed a-C films. G peak position and G peak dispersion show similar changes with pressure as the undoped films and little dependence on dopant percent. I_D/I_G ratio increases with pressure for 5% and 10% doping levels. 45

Figure 4-11. Raman data for boron doped pressed a-C films. 46
Figure 4-12. Schematic of voltage measurements given a constant current using the van der Pauw method. [47] 47
Figure 4-13. Ecopia SPCB-01 four point probe test set and pressed carbon film cemented to a glass microscope slide cover. 48
Figure 4-14. Resistivity test equipment. Keithley 225 constant current source, Keithley 181 Nanovoltmeter, and Ecopia SPCB-01 four point probe for van der Pauw measurements 49
Figure 4-15. Resistivity results for a-C, a-C:S, and a-C:B. 51
Figure 4-16. Surface graph of sulfur doped film resistivity highlights the much greater dependence on doping percent than pressure. 52
Figure 4-17. Surface resistivity graph of boron-doped films at all pressures and doping percentages. 54
Figure 4-18. Surface resistivity graph of boron-doped films at all pressures and doping percentages. 55
Figure 4-19 Principle of the Hall Effect. 58
Figure 4-20. Measurement schematic for the Hall effect. 58
Figure 4-21. GMW 5403 electromagnet and van der Pauw test set holder. 59
Figure 4-22. Hall voltages highlighting p-type behavior for a-C and boron doped films and n-type behavior for sulfur doped films. 60
Figure 4-23. Carrier concentration for undoped and sulfur doped films. 61
Figure 4-24. Carrier concentration for undoped and boron doped films. 62
Figure 4-25. Mobility data for undoped and sulfur-doped films. 63
Figure 4-26. Mobility data for undoped and boron-doped films. 63
Figure 5-1. Mating of p- and n-type materials in an unbiased PN junction results in the bands bending until the Fermi level is equal on both sides of the junction. [49] 65
Figure 5-2. Schematic of a photovoltaic device. Radioisotope voltaics use radio-active decay products instead of photons to produce electron hole pairs. [50] 66
Figure 5-3. Schematic of the four major assemblies of the PECVD reactor system. From left to right: electronics package; gas flow and precursor assembly; reactor chamber; and vacuum system. 69
Figure 5-4. Split view picture of PECVD reactor assembly.. 69
Figure 5-5. Precursor glass vial with stainless steel conflat flanges and Swagelok fittings. Not shown is the thermocouple, heating tape, or insulating aluminum foil. 70
Figure 5-6. Schematic view of the plasma enhanced chemical vapor deposition reactor chamber. 71
Figure 5-7. Reactor chamber made of a 4-way 3” cross using quick flanges. Precursors enter from left and vacuum pumps connect from the right. The RF plasma electrode is installed in the bottom flange. The top flange is removed to install substrates. Shown on the substrate holder is the substrate cartridge heater and thermocouple wire. 72

Figure 5-8. Substrate holder (top reactor flange). Shown is an aluminum mask and one carbon film.....72
Figure 5-9. Vacuum pumping system. Separate valves can isolate the reactor from the mechanical pump (on floor) or turbo pump (at left on stand).....73
Figure 5-10. I-V curve measurement system consisting of a laptop running Labview software which controls a Keithley 6517A Electrometer over a IEEE-488 interface.....76
Figure 5-11. Current-Voltage (I-V) characteristics of a nearly ideal, real PN junction diode where forward bias occurs for V>0. [49].....77
Figure 5-12. I-V curves of thermomechanically processed PN and PIN devices displaying lack of rectification and only resistor like behavior.....79
Figure 5-13. I-V curves for PECVD processed PN and PIN devices showing lack of rectifying characteristics and only resistor like behavior.....80
Figure 6-1 Bragg curve representing ionization in a target material due to a moving ion. The ion deposits most of energy near the end of the trail as represented by the peak. [53].....84
Figure 6-2. Postirradiation Hall effect data for undoped, sulfur, and boron doped films.....86
Figure 6-3. Raman results for the three irradiated films showing characteristics immediately following exposure to $\sim 10^{10}$ alpha particles and then after 5.5 days isothermal room temperature anneal.....88

List of Tables

Table Page

Table 2-A Properties of Carbon Allotropes. [15] 22
Table 2-B. Precursor materials. 28
Table 3-A. Experimental design factors for undoped carbon, dopant films. 31
Table 3-B. Summary of film growth parameters for resistivity measurements. 34
Table 4-A. Raman peak positions for carbon powders. 42
Table 4-B. Second order polynomial fit of sulfur doped film resistivity shown in Figure 4-16 52
Table 4-C. Wilcoxon signed ranks test results for differences in film resistivity 53
Table 4-D. Fit data for the full range surface resistivity graph of the boron-doped films shown in Figure 4-17. 54
Table 4-E. Fit data for the full range surface resistivity graph of the boron-doped films shown in Figure 4-18. 56
Table 4-F. Aggregate mobility data for undoped and doped films 62
Table 5-A. 2^{4-1} fractional factorial PN junction fabrication experimental design with four centerpoint runs 67
Table 5-B. PN junction, PIN device PECVD growth parameters 75
Table 5-C. Resistance of thermomechanically processed PN, PIN devices 78
Table 5-D. Results for PECVD fabricated PN and PIN devices 81

FABRICATION AND CHARACTERIZATION OF THERMOMECHANICALLY PROCESSED SULFUR AND BORON DOPED AMORPHOUS CARBON FILMS

1. Introduction

1.1. Motivation

There are a number of situations where small scale, high power density, reliable and long life power supplies that can operate across a wide range of environmental conditions would be useful or even mission critical. [1] Two of the most common uses are supporting space missions as well as the growing number of microdetectors, microsensors, and miniature vehicles. [2]

Deep space missions have a need for these power generation capabilities under extreme conditions, such as the ~200K temperatures encountered during recent Mars missions or ~600K temperatures often seen during missions in the inner solar system. [1] Conventional power generating and rechargeable storage devices are generally inefficient at very low temperatures and many devices fail at high temperatures. [3, 4]

While solar panel power generation may be an option for inner solar system missions not operating in the sun shadow, the needed light intensity falls rapidly beyond Mars for deep space missions. Other environmental challenges such as dust degradation of solar panel efficiencies can limit solar power usefulness even at Mars solar distance. [1]

There is also an increasing need for these types of power supplies for terrestrial applications. Advances in microelectromechanical systems (MEMS) and

microdevices such as microtransceivers, microchemical/biological sensors, micropressure sensors, and active radiofrequency identification systems also drive a need for small, long-life power sources with outputs ranging from microwatts to watts. [5]

The only currently available miniaturized power sources are electrochemical batteries and solar cells. Conversely, batteries tend to have short lives and are not well suited to temperature extremes. Solar cells on the other hand tend to have a low specific power not well suited to microscale devices.

Power supplies based on the energy from radioisotope decay could provide a possible solution to the capabilities described above. These power supplies could function reliably over long duration missions (months to decades) in extreme environments, without need for maintenance. While it is unlikely that power supplies based on radioactive materials would find widespread commercial use, there are a number of space and national security programs that could benefit from their development.

1.2. Background

The potential advantages of radioisotope power sources include life spans that could be tailored to last months to decades, specific power densities 100X higher than chemical batteries, and relatively insensitive to extreme environments.

Radioisotope power supplies are based on the conversion of radioactive decay energy into electrical energy. The decay products of interest are alpha particles, beta particles, and gamma/x-rays. Because gamma/x-rays penetrate so far

through materials (several cm), and deposit so little energy in the material, they are not feasible as the power producing mechanism and are primarily a dose concern that must be addressed when selecting an isotope as the radiation power source. Beta and alpha particles on the other hand typically only travel on the order of micrometers in solid/liquid materials and therefore deposit their energy over the distances ideal for microscale devices. Beta particles tend to have energy of 10s-100s of keV while alpha particles generally are 1-10 MeV.

Critical to the feasibility of radioisotope voltaic power sources is efficient nuclear-to-electrical conversion and high tolerance of the device to ionizing radiation. There are generally four mechanisms to convert decay particle energy into electrical power: generate electron hole pairs (EHP) in semiconductor devices such as PN junctions, Schottky diodes, or PIN diodes; generate photons in a phosphor then convert photons to electricity similar to a solar cell; generate EHP in a material with charge separation due to contact work function differences; and conversion of decay heat using thermoelectric materials. [6]

Much of the previous work on radioisotope voltaics has been focused on direct energy conversion by depositing the particles in the depletion region of PN junctions and Schottky/PIN diodes made from the common inorganic crystalline column III/V, and II/VI semiconductors. The alphavoltaic devices in particular have been unsuccessful in the long term due to the highly energetic alpha particles damaging the crystal lattice and degrading the power output, often within hours. Many groups have attempted to improve the radiation hardness of these junction

devices by developing novel device architectures such as lateral junction nipi devices or using radiation resistant solar cell materials such as InGaP. [2, 3, 6, 7] While these devices have shown some improvement in damage resistance, they still do not have acceptable life spans and many are sensitive to temperature extremes where the device may break down due to thermal decomposition. There has been less work done on evaluating amorphous radioisotope voltaics, which could provide an opportunity to reduce the effects of ionized particle damage.

Another conversion approach uses a phosphor, one version of which is inherently rad hard quantum dots, to convert radioisotope energy into photons. These photons are then converted to electricity via the photoelectric effect in a semiconducting junction device tuned to the energy level of the photons. While this approach protects the junction from lattice damage, the additional conversion step extracts a significant efficiency penalty. [6, 8]

More recently, work has been done on generating power by placing a radiation source in a liquid semimetal (gallium) sandwiched by contacts of different metal (iridium and zirconium). [9] The work function of the different metals provides a voltage across the semimetal that separates the EHP generated by the moving alpha particle. This liquid semimetal continually “heals” the ionization damage and does not suffer degradation in power due to material changes. Packaging and manufacturing are complicated for liquid devices however, particularly in low temperature environments. Efficiency data is sparse for this type of device to date.

While radioisotope thermo-electric generators (RTGs) have been used for deep space missions and unattended terrestrial remote sensors, the low energy conversion efficiency and specific power characteristics of RTGs has limited their use to relatively large systems requiring more than 10s of watts. There are efforts to shrink the overall package size of RTGs but the state of the art is still expected to be on the order of >1cm^3 which is too large for microscale devices. [1]

1.3. Critical Properties For Effective Radioisotope Voltaics

The optimal radioisotope voltaic device would: have a high energy conversion efficiency and specific power output; suffer no performance degradation due to damage from the ionized particles; work over a wide range of temperatures; use non-toxic materials; and be produced at low cost. In reality, there have been and will likely continue to be trades made between cost, efficiency, and life span.

Energy conversion efficiency in an radioisotope voltaic device is a function of the current and voltage generated in the device for a given amount of energy deposited by the particles. In general, the conversion efficiency and power output is proportional to both the number of EHP generated in the particle ionization trail and likelihood that those charged particles can be separated to contribute to a short circuit current before recombining or being trapped in defects in the device. In photovoltaic solar cells, a potential difference, typically 1-3 volts, across a PN junction provides the electric field that separates the EHP. [10] This mechanism can also be applied to radioisotope voltaic devices.

At this relatively low potential difference, it is critical that EHP recombination and charge trapping be minimized in order to maximize the current and power output of the device. Recombination occurs when an electron and hole annihilate each other in a material and reduce the current output. This recombination can occur immediately at the ionization site or as the charge moves through the material. A measure of merit for how well charge moves through a material prior to recombining is to assess the diffusion length *L*:

$$L = \sqrt{\frac{kT}{q}\mu\tau} \qquad \text{(Equation 1-1)}$$

where k is Boltzmann's constant, T is the temperature, q is the charge, μ is the mobility of the electrons and holes in the specific material, and τ is the average lifetime of a minority carrier surrounded by majority carriers for that material. [11] We can infer from Equation 1-1 that the ways to reduce recombination are to choose a material where L is large or where the device size is less than L. Maximizing the mobility μ is critical to maximizing L. Traditional semiconducting materials such as crystalline silicon or gallium arsenide have diffusion lengths longer than the micrometers that alpha particles move in materials so are generally not significantly limited by recombination. [11] Nontraditional materials such as organics recently tested as photovoltaic cells only have diffusion lengths on the order of nanometers so require novel device architectures to minimize the distance EHP must travel prior to moving into a conduction channel. [12]

Charge trapping occurs when an electron or hole moving through the material are stopped at an impurity site or defect in the material. Besides the reduction in current and power when the charge is trapped and stops moving, the now relatively fixed charge can induce space charge effects that adversely affect the flow of nontrapped charges. Defect introduction and reduction in power output is a major consideration for alphavoltaic devices in particular. The energetic, ionized alpha particles can significantly degrade the structure of the material they are traveling through, particularly at the end of the ionization trail where they deposit the most energy. Highly ordered devices such as crystalline silicon PN junctions can have the alphavoltaic power output degrade by > 90% in as little as hours. [2] Alphavoltaic devices have also been made with more radiation tolerant crystalline materials such as diamond, SiC, InP, and InGaP. These devices have improved defect resistance but still typically lose over half of their power output due to device degradation. [2] Amorphous or polycrystalline materials on the other hand are likely to have slightly lower efficiency initially but are likely less susceptible to radiation damage and often cost less to manufacture.

As previously mentioned, stability under a wide temperature range is a highly desirable property for a radioisotope voltaic. Most semiconducting materials generally perform well in the 200-400K temperature range but begin to suffer performance degradation and ultimately failure as the temperature approaches 600K. At these high temperatures, traditional thin film inorganic device layers tend to interdiffuse and lose the desired electrical properties or become overly

conductive. [1, 11] Amorphous materials with high activation energies such as carbon may offer improved resistance to high temperature degradation.

While energy conversion efficiency, radiation resistance, and temperature insensitivity are the most important criteria when selecting the materials and design for a radioisotope voltaic, there are other properties to consider. Ideally, the materials would be non-toxic and the design would have a low manufacturing cost. The design should also be scalable in size and suitable for incorporation of different radioisotopes based on required power, lifespan, and cost.

1.4. Problem Statement

Can nanocarbon precursors be doped and thermomechanically processed into films suitable for use in PN junctions or PIN diodes to form efficient, radiation hard radioisotope voltaics?

1.5. Research Methodology

This research was conducted along two parallel paths. After an initial screening experiment to choose a carbon nanopowder precursor and pressing of undoped and doped films, one path was the characterization of those films while the parallel path was attempting to fabricate PN junction and PIN devices. A limited number of alpha particle irradiated film samples were then characterized to note changes in properties.

The first step was to conduct an initial screening experiment using a heated hydraulic press to determine whether graphitic, amorphous, and diamond nanopowders could be compressed into mechanically stable films. The film bonding

properties were then characterized using Raman spectroscopy. Once a suitable precursor was found, the next step was to introduce sulfur as a potential n-type dopant and boron as a p-type dopant.

After these powders were then pressed into films using a range of pressures (0.3-5 GPa) and dopant percent (2.5-10.0%), they were characterized using the van der Pauw technique for Hall Effect measurements as well as Raman spectroscopy.

In parallel with the film characterization, PN and PIN devices were fabricated to determine whether they had rectifying properties.

The final step included the alpha irradiation of a limited number of undoped a-C, and boron and sulfur-doped films with Hall Effect and Raman characterization of those films.

2. Amorphous Carbon Films

2.1. Introduction

2.1.1 Carbon Materials.

Carbon exists in a variety of allotropes, the most familiar of which are graphite and diamond (see Figure 2-1 and Table 2-A). [13]

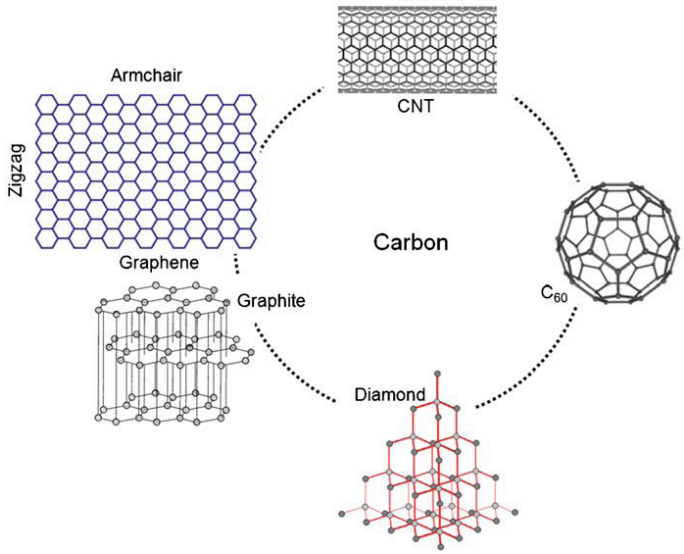

Figure 2-1. Common allotropes of carbon. CNT are carbon nanotubes. [13]

Graphite consists of threefold coordinated sp^2 bonds with equidistant σ bonded nearest neighbors 120° apart in a plane as shown in Figure 2-2. [14] The fourth valence electron of the sp^2 atom then forms a weak π bond normal to the plane with an adjacent plane π bond. Structurally, graphite can exist in either hexagonal or rhombohedral form. Because of the planar sp^2 bonding, graphite is metallic and has high electrical and thermal conductivity in the plane and much smaller conductivity perpendicular to the plane. The high conductivity of graphite results from having no bandgap. Graphite is mechanically soft due to weak interplanar bonding forces.

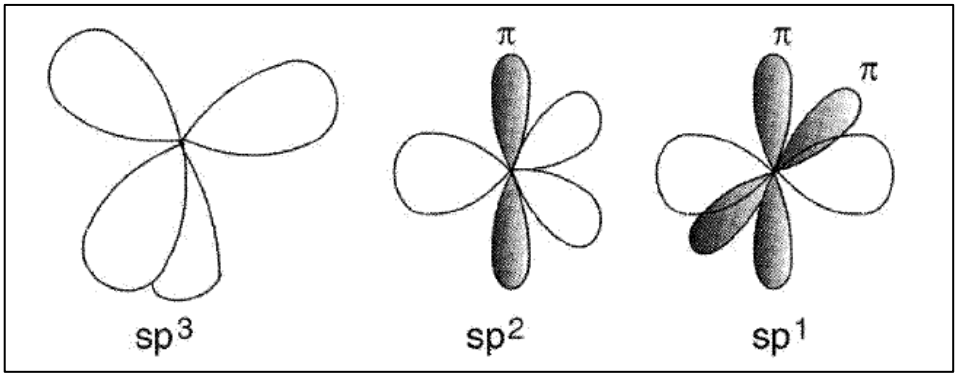

Figure 2-2. sp^3, sp^2, sp^1 hybridized carbon bonding. sp^3 bonding, as in diamond, occurs when the four valence electrons bond tetrahedrally with adjacent atoms via σ bonds. sp^2 bonding, as in graphite, occurs when three valence electrons form σ bonds in the plane and one electron forms a π bond normal to the σ bond plane. sp^1 bonds occur when two valence electrons form σ bonds along the ± x axis while the other two electrons form π bonds along the y and z axis. [15]

Diamond consists of fourfold coordinated sp^3 bonds, all of which form strong σ bonds with adjacent atoms. While a hexagonal form (Lonsdaleite) exists, the much more common form is cubic as shown in Figure 2-1. Diamond has low electrical, but very high thermal conductivity; has a wide bandgap of 5.5 eV; and is among the hardest known substances. [15]

Table 2-A Properties of Carbon Allotropes. [15]

	Crystal structure	Hybridization	Conduction type	Band gap (eV)	Work function (eV)
a-C	–	sp^3+sp^2	Semiconductor	0.2–3.0	4.9
Diamond	Cubic	sp^3	Insulator	5.5	5.45
Graphite	Hexagonal	sp^2	Conductor	0	5.0
Fullerene (C_{60})	Cubic	sp^2+sp^3	Semiconductor	1.6	4.6–5.0
CNT	Cylindrical	sp^2+sp^3	Metallic/semi-conducting	0.3–2.0	4.5–5.1
Graphene	–	sp^2	Semi-metallic/semi-conducting	0–0.3	5.0

Amorphous carbon (a-C) has little to no macroscopic crystal structure or long-range order and consists of variable percentages of graphitic sp^2 and diamond-like sp^3 bonded carbon with or without hydrogenation to passivate dangling bonds.

The key parameters in defining a-C are the percent sp^2 content, clustering of sp^2 bonded atoms, orientation of sp^2 phase, the cross-sectional nanostructure, and H or N content. [16] Within an a-C sample, there will be a distribution of bond type, number of clusters, and size of clusters that affect the mechanical, electrical, and optical properties.

One of the most intriguing allotropes of carbon is tetrahedral amorphous carbon (ta-C), also known as diamond like carbon (DLC). DLC is amorphous carbon with a high percentage of sp^3 bonds as shown in Figure 2-3. Depending on the exact percentage of sp^3 and sp^2 bonds, the material behaves more like a semiconductor but with excellent thermal conductivity. DLC is also very hard like diamond but the lack of long-range order allows the material to remain flexible due to a lack of crystalline fracture planes.

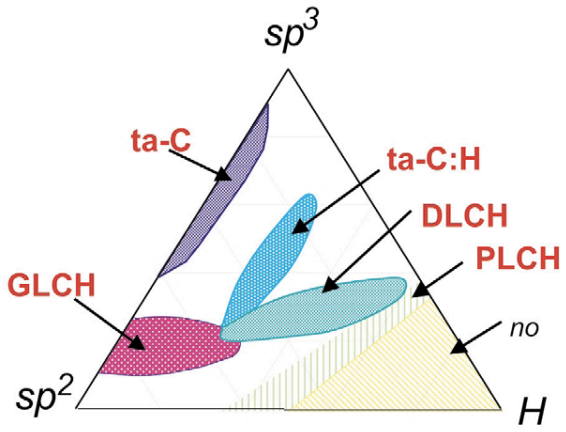

Figure 2-3 Amorphous carbon ternary phase diagram. sp^2 corresponds to graphite, sp^3 to diamond, and H to hydrocarbons. GLCH and PLCH are graphite and polymer like hydrogenated carbons. [16]

Graphite is the most stable allotrope and is thermodynamically favored at the standard temperature and pressure as shown in the phase diagram at Figure 2-4.

While it is not technically true that “diamonds are forever” as claimed in the commercials, diamond is clearly metastable at STP and at industrial conditions where diamonds are frequently used. This metastability results from very large activation energies to move between phases and thus graphite and diamond allotropes are metastable well into the temperature and pressure region of the other phase. [14]

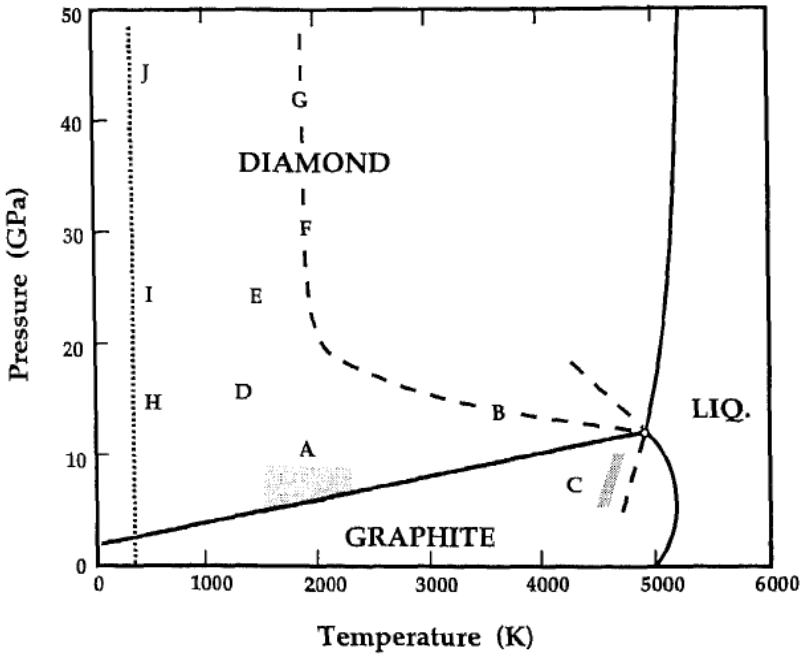

Figure 2-4. Pressure-temperature diagram of carbon. This work will focus on the area below 600K and 5GPa. See reference for full description. [14]

The ideal material for voltaic cells would have a small bandgap (~1-2eV), good thermal conductivity and semiconductor characteristics, be mechanically hard but not brittle, and resistant to degradation from radiation. Neither graphite nor diamond by themselves meet all these needs. An amorphous carbon with a tailored

mix of graphitic sp^2 and diamond-like sp^3 could be optimized to meet the criteria and is the underlying principle behind this research.

While DLC films grown by CVD have excellent mechanical properties, there are a number of issues with the electronic properties such as poor doping response, large density of mid-gap states, wide band tails, and low carrier mobility. [17] DLC films are generally considered to have <40% sp^2 content as shown in Figure 2-3. As shown in Figure 2-5, ~80% sp^2 percentage results in carbon with an optical gap of ~1eV. Therefore a film with 40-100% sp^2 bonding may have the desired properties.

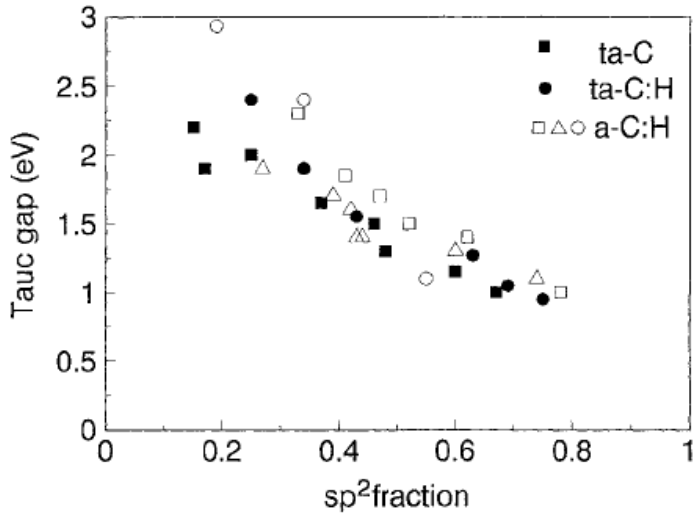

Figure 2-5. sp^2 fraction vs. experimental optical gap for disordered carbons. The optimal gap for a voltaic cell is ~ 1eV. [15]

Ideal sp^2 clusters are moderately sized and evenly distributed throughout the bulk material to maximize consistent tunneling and hopping conduction while keeping the bandgap relatively small. Controlling this distribution has been difficult using CVD methods and attempts to use thermal annealing to adjust the size results

in a cluster size increase. [16] There is no known data on thermomechanically processed carbon cluster size or manipulation.

2.1.2 Carbon Doping.

Doping semiconductor materials allows manipulation of the resistivity of the material and the hole and electron population and mobility as needed for specific applications. In order to avoid lattice-matching issues between different types of materials, a semiconducting material should ideally be able to be doped both n- and p-type in order to form effective PN junction devices. n-type materials have excess electrons while p-type materials have excess holes to act as carriers.

Graphite is metallic and doesn't need to be doped to be conductive. Crystalline diamond however, is a wide bandgap semiconductor and needs to be doped in order to reduce the bandgap to be suitable for most applications. Unfortunately, diamond is typical of many wide gap semiconductors and only dopes easily to one polarity because the dopant levels are too deep, dopant solubility is low, or auto-compensation occurs. [15] Using CVD or ion implantation, crystalline diamond is easily doped p-type by boron but poorly n-type by nitrogen and phosphorus.

Amorphous carbons, to include DLC, deposited by CVD or other high energy techniques are weakly p-type prior to any attempt at doping. [18] n-type doping of DLC using these high energy techniques has been successful with nitrogen [18-22], phosphorus, [23] and sulfur. [24, 25] Similar to crystalline diamond, amorphous carbons have been doped p-type with boron. [26] Palladium has also been used as a

dopant, resulting in a quasi-intrinsic semiconductor with a small bandgap of ~1.1eV that produces carriers under illumination. [27] To date, there are no known attempts at doping amorphous carbon films using thermomechanical processing.

2.1.3 Thermomechanical Processing.

Thermomechanical processing, also known as hot pressing, is the application of heat and pressure to a substance in order to cause a change in electronic or material properties at a temperature below the melting point of the material. From the phase diagram at Figure 2-4, we can deduce that the transition pressure function P(T) is given by:

$$P = 1700 + 2.06T \qquad \text{(Equation 2-1)}$$

where T is in °K and P in MPa. [28] As an example, at 1000K graphite pressed at a pressure > 3760MPa should convert to diamond and due to metastability, likely remain in that state after returning to low pressure and temperature. The reality is somewhat more complicated as graphite is also metastable in the diamond phase regime. It is most likely that there will be some conversion of sp^2 graphite to sp^3 diamond resulting in a amorphous or polycrystalline material. Thermomechanical processing has been used successfully to grow organic semiconductor thin films. [29] These organic molecules tend to have high molecular mobility and form plastic crystals under pressure, without lubricant, due to their low entropy of fusion. Graphite and diamond however have a significantly higher entropy of fusion than these molecules and may need to have a lubricant during pressing to allow molecular rearrangement as is common with many ceramic nanopowders. [30]

2.2. Film Pressing Apparatus

2.2.1 Precursor Materials.

Precursor materials consist of a mixture of a variety of potential dopant materials and carbon nanopowders as shown in Table 2-B.

Table 2-B. Precursor materials.

Sigma Aldrich Item Number	Description
699624	Mesoporous Graphitized Carbon Black <500nm
636428	Diamond Nanopowder <50nm
633100	Amorphous Carbon <50nm
13803	Sulfur
378119	Boron Carbide (B_4C)

Sulfur powder is typically found as the S_8 cyclooctasulfur allotrope as shown in Figure 2-6. Sulfur has a melting point of ~115°C and a very high resistivity of $\sim 10^{13}$ Ω-cm.

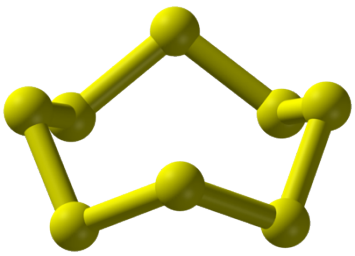

Figure 2-6. Cyclooctasulfur S_8 ring. [31]

The boron carbide precursor used in this research is nominally B_4C as shown in Figure 2-7. This form of boron carbide consists of a 15-atom unit cell with 12 atoms in an icosahedra and three inter-icosahedra atoms connecting equatorial regions of nearby icosahedra. The structure can vary within a crystal such that boron can replace carbons in the chain and carbon can replace boron in the

icosahedra. Regardless of the exact structure, boron carbide is an electron deficient material that is often used as a p-type dopant.

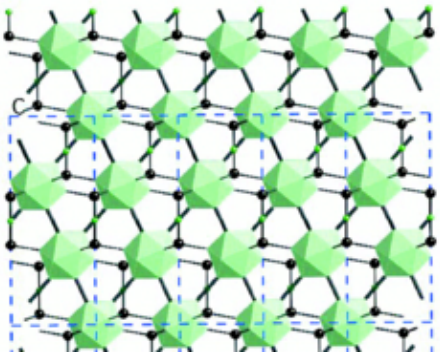

Figure 2-7. Boron carbide (B_4C) nominal structure. [32]

2.2.2 Powder Mixing

In this research, three levels of dopant mixing (2.5at%, 5at%, 10at%) of boron and sulfur mixed with a-C was investigated. Appropriate amounts of B_4C and sulfur powders were weighed on a μg scale with a-C prior to mixing. Each of the powders was mixed for 5 minutes in the Wig-L-Bug grinder shown at Figure 2-8 using an agate ball and cylindrical pestle to break up crystals and maximize particle size uniformity.

Figure 2-8. Wig-L-Bug grinder/mixer.

2.2.3 Film Pressing

Films were grown using the PHI-Tulip cooled/heated, programmable 30-ton press shown at Figure 2-9. The press can reach temperatures of ~300C and pressures of 5GPa when pressing a 8mm diameter film.

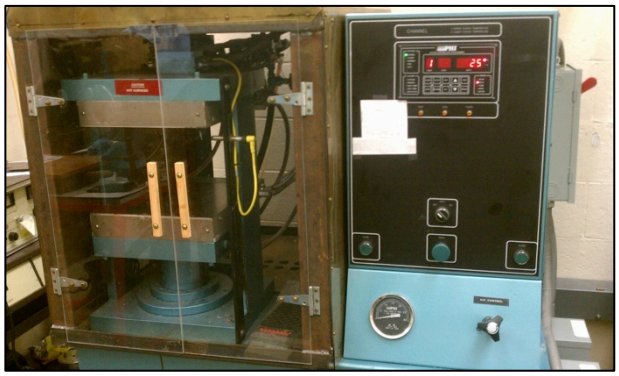

Figure 2-9. PHI-Tulip heated/cooled programmable 30-ton hydraulic press.

3. Film Growth Procedures

3.1. Undoped Films

An initial screening study using a 18 run (16 + 2 centerpoints) factorial experimental design was conducted to determine which of the processing factors have the greatest impact on the characteristics of the undoped carbon films. As shown in Table 3-A, the four factors are substrate temperature, pressure, % diamond (vice graphitized carbon black nanopowder) in the precursor powder, and pressing time. The measured response was intended to be the film resistivity. The temperatures and pressures were chosen so that at the higher levels, the carbon would theoretically cross into the metastable diamond portion of the phase diagram (Figure 2-1) and would change the sp^2-sp^3 ratio and the electronic properties. The % diamond ratios were similarly chosen to enable variations in the sp^2-sp^3 ratio.

Table 3-A. Experimental design factors for undoped carbon, dopant films.

Run	X1	X2	X3	X4	Actual Run Order
1	0	0	0	0	1
2	-1	-1	-1	-1	5
3	1	-1	-1	-1	2
4	-1	1	-1	-1	4
5	1	1	-1	-1	13
6	-1	-1	1	-1	8
7	1	-1	1	-1	17
8	-1	1	1	-1	12
9	1	1	1	-1	15
10	-1	-1	-1	1	9
11	1	-1	-1	1	3
12	-1	1	-1	1	14
13	1	1	-1	1	7
14	-1	-1	1	1	6
15	1	-1	1	1	11
16	-1	1	1	1	16
17	1	1	1	1	10
18	0	0	0	0	18
	-1	0	1		
X1 (% diamond)	50	75	100		
X2 Temp (C)	30	140	250		
X3 Pressure (MPa)	200	2600	5000		
X4 Time(min)	10	20	30		

The films were initially grown using 0.001” PTFE release films (Fluoro Plastics) on glass microscope slides similar to the methods Baklar, et al used with large organic molecules. [29] Using this technique, the pressed nanopowders did not form cohesive films and the powder typically stuck to the PTFE release films. The films also tended to fracture and the microscope slides cracked. As the runs continued, the procedures evolved to include trying PTFE mold release spray

instead of the compressible PTFE film, ethane as a lubricant, and using various metal substrates to improve film quality. During this time, a-C powder was added as a potential precursor and several films were pressed over the same range of pressures and times as the GCB and nanodiamond films.

The most cohesive films, from a uniform thickness and subjective strength perspective, were found by pressing unlubricated a-C powders directly between 0.25mm Ni substrates. 70mm stainless steel vacuum chamber plugs were used as pusher plates to protect the press platens as shown in Figure 3-1.

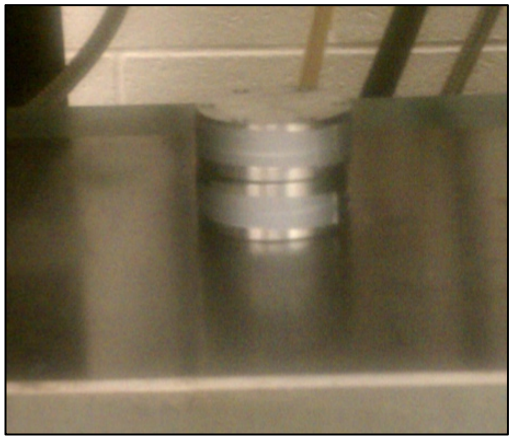

Figure 3-1. 70mm stainless steel pusher plates used to protect press platen.

Ultimately, baseline films were successfully grown using a-C powder across the entire range of temperatures and pressures. The films grown using any nanodiamond and graphitized carbon black, even when mixed with a-C, were unsuccessful from the perspective that they were very brittle and fractured easily enough that they were essentially impossible to handle for any characterization

testing. Resistivity measurements of these films were not taken as they were no longer needed for the screening.

3.2. Doped Film Growth

There were several potential dopant materials considered. In order to minimize the number of processing variables, one of each type of dopant was chosen. For p-type films, aluminum (Al_4C_3) and boron (B_4C) were considered. Boron was chosen primarily because it has been a successful dopant using other processing techniques and does not have the safety issues associated with using aluminum carbide in a water-cooled press. [26, 33-39]

For n-type films, sulfur was selected as it has also been a successful dopant using other processing methods. [24, 25, 40-44]

The initial goal was to determine if doping changes the resistivity of the a-C films and whether the change was significant by using Wilcoxon Signed Ranks Test (WSRT). From the initial pressing of a-C films, it was subjectively determined that the films that were pressed for 30 minutes were more robust and less likely to break during handling than the 10-20 minute films so a 30 minute press time was fixed for the next experimental design.

Similarly, it appeared that the films pressed at higher temperatures were less fragile than the room temperature films. A range of temperatures was initially chosen but even at the lowest 2.5% doping level, temperatures above the sulfur melting point resulted in unusable films and a significant mess. Thus, the temperature was fixed at 109°C, 95% of the sulfur melting point. While the boron

doped films could be pressed at higher temperatures, the same temperature as sulfur was chosen to facilitate direct comparison of changes in film properties.

The 30-ton hydraulic press has a maximum of ~5GPa of pressure when pressing a 8mm diameter disk of powder. This is sufficient pressure to cross into the diamond portion of the phase diagram. As the WSRT requires a minimum of 6 points for comparison for a 95% confidence level, a pressure range of 0.3, 1, 2, 3, 4, 5 GPa was selected. In order to determine the impact of dopant percentage on resistivity, mixtures of a-C with sulfur and B_4C at 2.5, 5, and 10 at% were pressed. The resistivity experiment parameters are summarized in Table 3-B.

Table 3-B. Summary of film growth parameters for resistivity measurements.

Precursor	Dopant	Doping Percent	Time (min)	Temperature (C)	Pressure (GPa)
a-C nanopowder	None, S, B_4C	2.5, 5.0, 10.0	30	109	0.3, 1.0, 2.0, 3.0, 4.0, 5.0

4. Amorphous Carbon Film Characterization

4.1. Raman Spectroscopy

4.1.1 Introduction

Raman spectroscopy is the standard nondestructive characterization method for amorphous, nanocrystalline, and crystalline carbons. [45] The technique is based on the inelastic scattering of monochromatic light, typically from a laser, and measurement of the shift in the frequency of the scattered light. The predominant scattering occurs from the ground state through a virtual energy state to a higher energy vibrational state characteristic of the measured material. The emitted

photon will have shifted to a lower frequency known as the Stokes shift as shown in Figure 4-1. A schematic of a Raman spectrometer is shown at Figure 4-2.

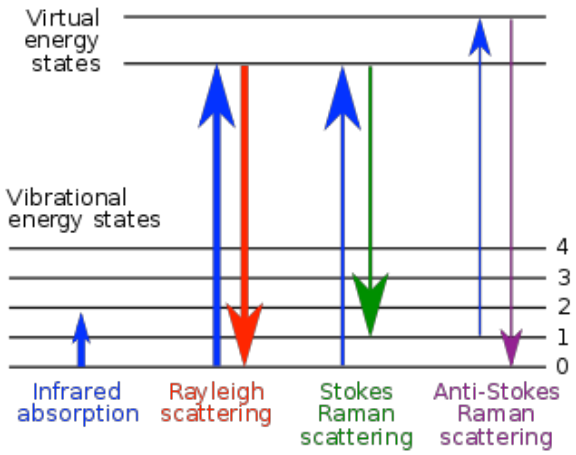

Figure 4-1. Schematic of inelastic scattering that is the basis of Raman spectroscopy. Unheated carbon measurements are in the Stokes scattering regime. [45]

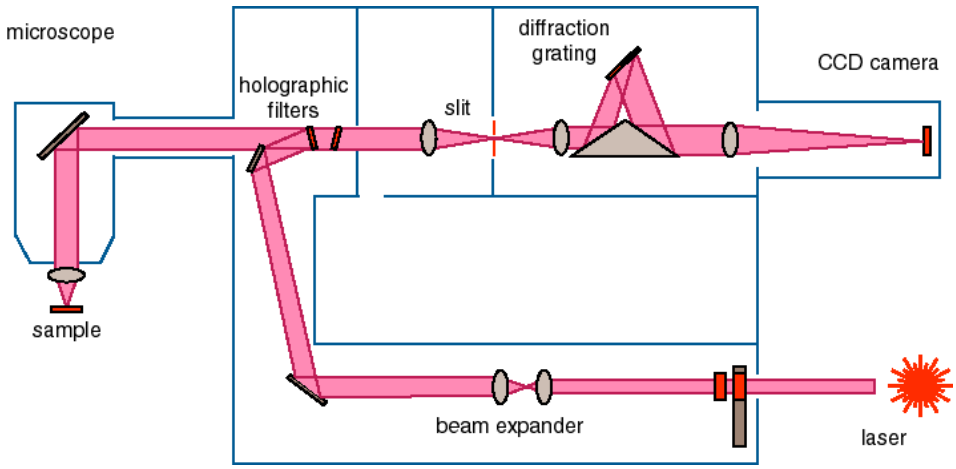

Figure 4-2. Schematic of a Raman spectrometer.

Raman spectra of carbon powders are routinely assessed using the Ferrari-Robertson model shown at Figure 4-3. [45] In this model, the D ("disorder") peak at ~1355 cm^{-1} is representative of the A_{1g} breathing mode which is only allowed in the

presence of disordered sixfold aromatic rings. The G ("graphitic") peak, which lies in the range of 1500-1630 cm^{-1}, represents the in-plane stretching of the sp^2 bonds between aromatic or olefinic molecules. [45] For films of these materials, changes in clustering and disorder generally result in changes to the Raman spectra as shown in the model at Figure 4-3. Visible/NIR Raman is most useful for directly determining the sp^2 content of the film as it's interaction cross section is 50-200X that of sp^3 bonded atoms. While not directly observable with the ubiquitous 514nm Raman, the sp^3 content can be inferred from changes in the spectra.

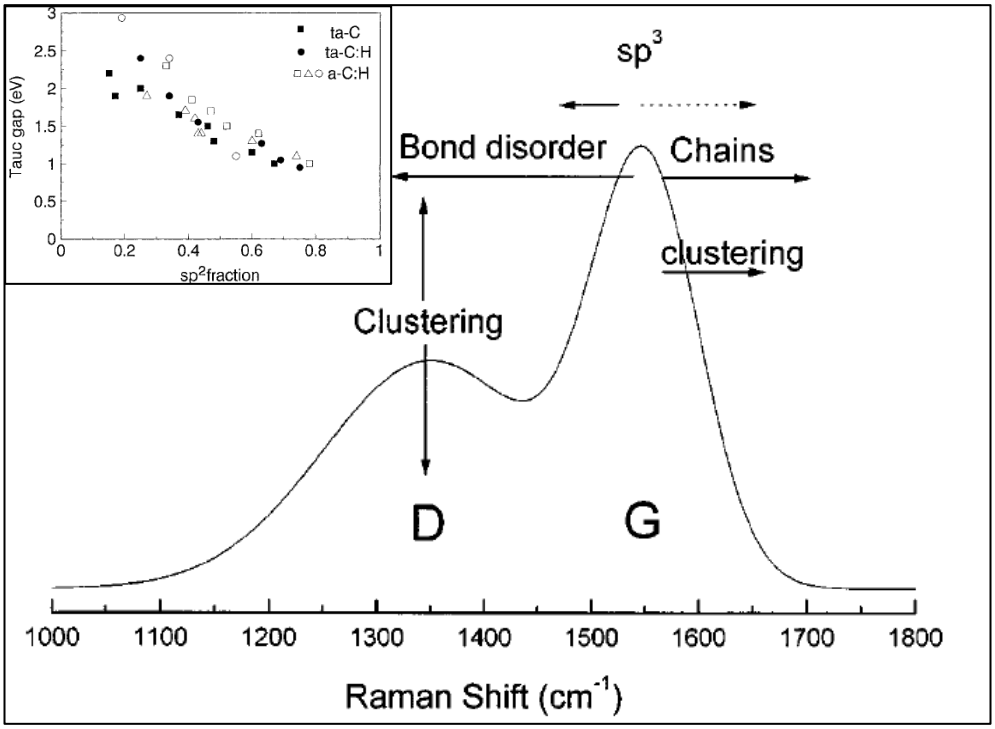

Figure 4-3. Schematic of sp^2 bonding influences on 514nm Raman spectra of disordered carbons. [45]

Two other key Raman assessments of disordered carbons, shown in Figure 4-4, are the I_D/I_G ratio and the G peak dispersion. This model, tied in with the Tauc

gap data from Figure 4-3 (inset), allows us to use Raman spectroscopy to understand structural changes as the powders are thermomechanically pressed and the first order effect on bandgap.

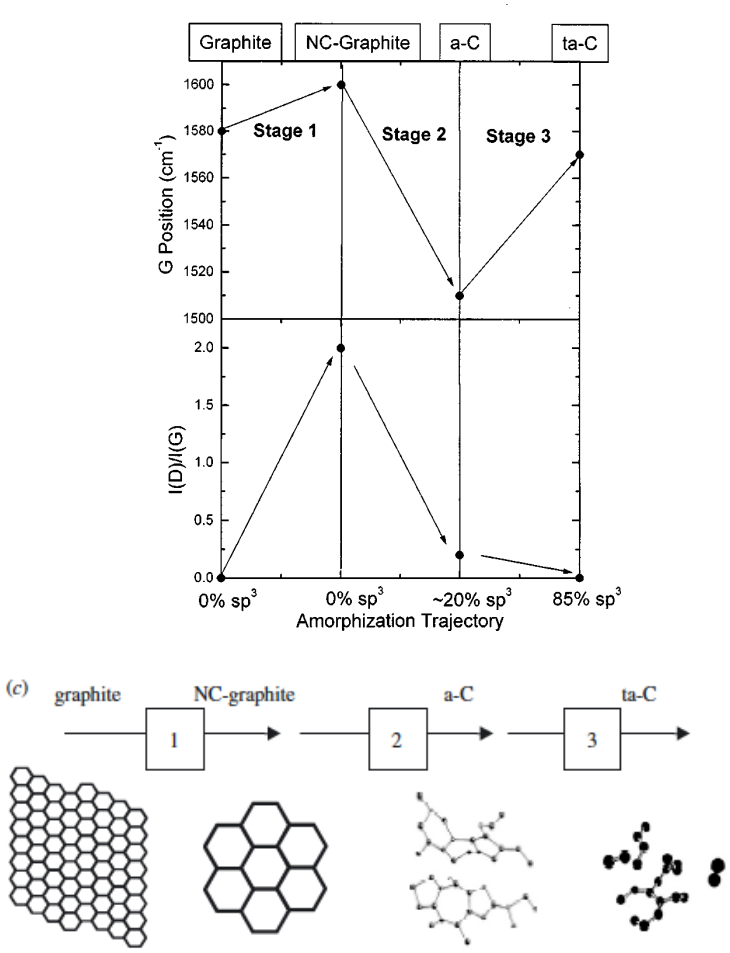

Figure 4-4. Schematic variation of the I_D/I_G ratio and the G peak dispersion. [45]

Using different Raman excitation energies on the same sample can also provide information on the sp^2 configuration of the film by assessing the G peak dispersion defined in (Equation 4-1. [45]

$$G\ disp\ \left(\frac{cm^{-1}}{nm}\right) = \frac{G\ pos\ (514nm) - G\ pos\ (785nm)}{(785 - 514)nm} \qquad \text{(Equation 4-1)}$$

G peak dispersion is used to assess the sp^2 clustering of a film. An increase in G peak dispersion always represents disordering while a decrease always means ordering of the sp^2 clusters.

4.1.2 Apparatus and Procedure

Raman spectra were obtained for the three carbon precursor powders and doped and undoped films using the Renishaw InVia spectrometer shown at Figure 4-5. The spectrometer has lasers with 514nm, 633nm, and 785nm wavelength.

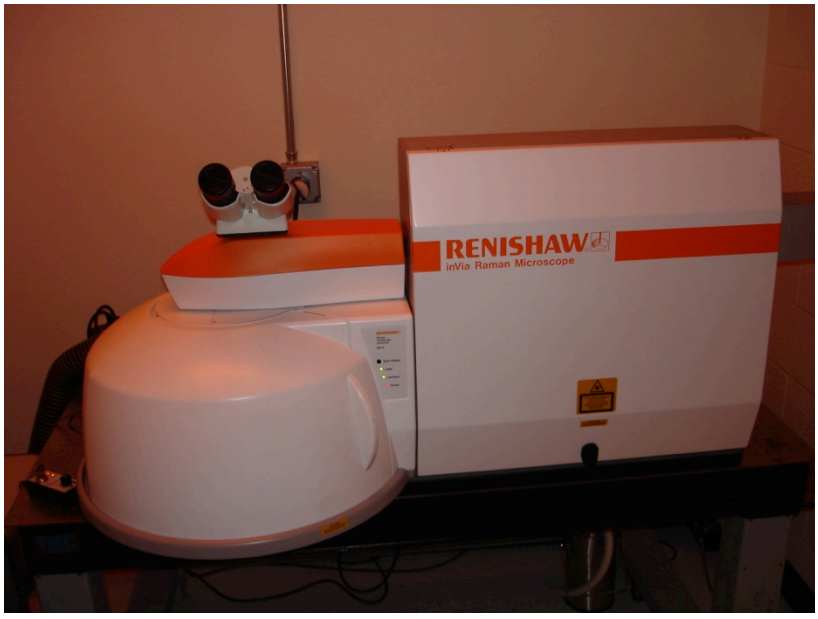

Figure 4-5. Renishaw InVia Raman Spectrometer. The spectrometer has 514nm, 633nm, and 785nm lasers to cover a range of excitation energies.

The powders/films were placed on a cleaned microscope slide and then placed under the Raman microscope with 100X lens selected. Spectra were taken at both 514nm and 785nm using the 1800g/mm grating over wavenumbers of 100-3200cm^{-1}. The 514nm laser was at ~50% power on the analog dial power switch while the 785nm solid state laser was driven at 1% power through the Raman software. Exposure times with 10 second accumulation provided the best balance of noise vs throughput. Critical to good results was ensuring the 100X microscope lens was well focused.

The raw spectrum data was imported into OriginPro 8.5.1 for processing using the peak analyzer function. A user-defined baseline was selected to subtract the fluorescence. The G peak was fit with a Breit-Wigner-Fano peak and the D peak with a Lorentzian peak per Ferrari-Robertson. [45] The peak fits resulted in a adjusted R square value of >0.98.

4.1.3 Film Imaging

A microscopic view of the images is shown at Figure 4-6. It appears from both 5X magnified images that there are parallel band type structures that are likely related to stress in the film from being pressed. At 100X magnification we see the short-range disorder in the film.

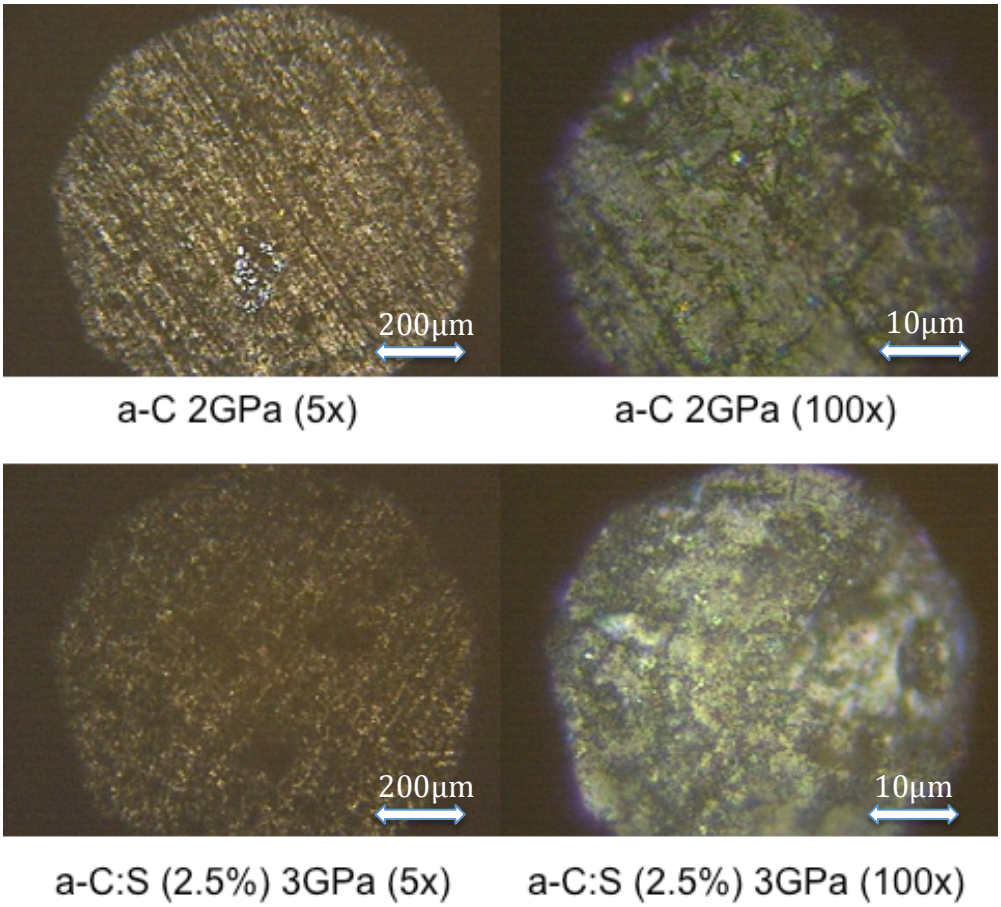

Figure 4-6. Film images taken through the 5X and 100X Raman microscope objective lenses.

4.1.4 Carbon Nanopowder Raman Baseline

From the results in Figure 4-7 and Table 4-A, we can see that the a-C powder from Sigma Aldrich is essentially a stage 1 nanographite in the Ferrari-Robertson model at Figure 4-4. The G peak shifts from the crystalline graphite peak at 1580 cm^{-1} to 1595 cm^{-1} while the D peak shifts up due to nanoclustering of the aromatic rings. This precursor is almost entirely composed of sp^2 aromatic rings.

The graphitized carbon black (GCB) from Sigma Aldrich fits in stage 2 of the model. The shift to lower wavenumbers of the G peak and reduced D peak height are indicative of an increased number of sp^2 chains and resultant amorphization but is still primarily an aromatic ring structure.

The nanodiamond powder D peak is centered on the crystalline diamond peak of 1332 cm^{-1}, which highlights the increased sp^3 nature of the precursors. The shift of the G peak to increased wavenumbers however leads us to believe there is a sp^2 component in the form of olefinic chains between nanodiamond clusters. [45] These initial Raman studies led to the use of the GCB and diamond nanopowders for the first films as they most clearly had either sp^3 atoms or sp^2 chains that might enable easier tailoring of the films properties. As previously discussed however, the inability to press cohesive films with GCB or nanodiamond led to the exclusive use of the a-C nanopowders.

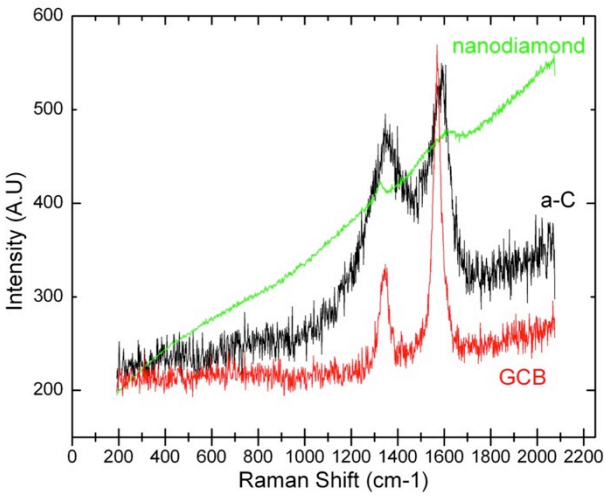

Figure 4-7. Baseline Raman spectra of a-C, graphitized carbon black (GCB), and nanodiamond powders using a 514nm laser.

Table 4-A. Raman peak positions for carbon powders.

Precursor	D peak position (cm^{-1})	G peak position (cm^{-1})	I_D/I_G
a-C	1345	1595	0.8
GCB	1345	1568	0.3
Nanodiamond	1332	1607	1.0

4.1.5 Thermomechanically Processed Undoped Carbon Raman Results

The Raman spectra for the pressed carbon films are shown in Figure 4-8 and Figure 4-9. Figure 4-8 does not show the details of peak fitting but is representative of little gross change in the properties of the films. From Figure 4-9, we see that the G peak position generally decreases as pressure increases while the I_D/I_G ratio generally increases with pressure after an initial dip from the powder level. G peak dispersion is very low (~10% of typical a-C) and implies the film is largely nanographitic. [46] The slight decrease in G peak position and approximate saturation at 1580cm^{-1} by itself would indicate slight amorphization away from nanographite. Interestingly, in these films the I_D/I_G ratio moves in opposition to the G peak position, which is different then the Ferrari-Robertson model.

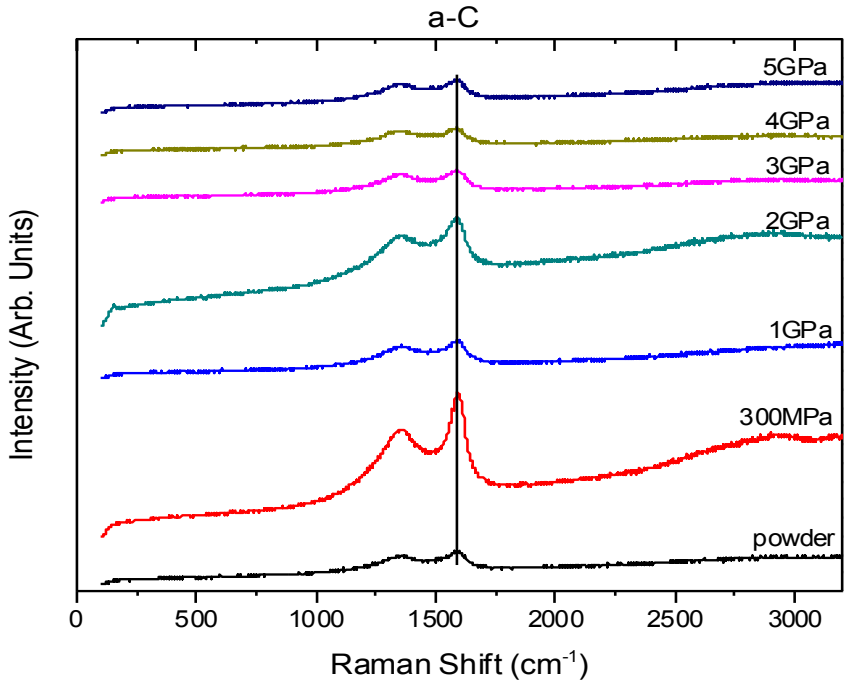

Figure 4-8. 514nm Raman spectra raw data of thermomechanically pressed a-C showing no significant change in G peak position with pressure.

The disparity arises from the assumption built into the Ferrari-Robertson model that films are uniformly nanocrystalline. From first principles, the G peak is due to bond stretching/distortion in both sp^2 chains and rings while the D peak is due only to sp^2 ring breathing modes. The decrease in G peak position and I_D/I_G may be due to the act of pressing the film causeing clustering in the nanopowder precursor with it's dangling bonds while simultaneously increasing the distortion of the existing sp^2 rings. The bond distortion would also explain the internal stress in the film that makes them so brittle.

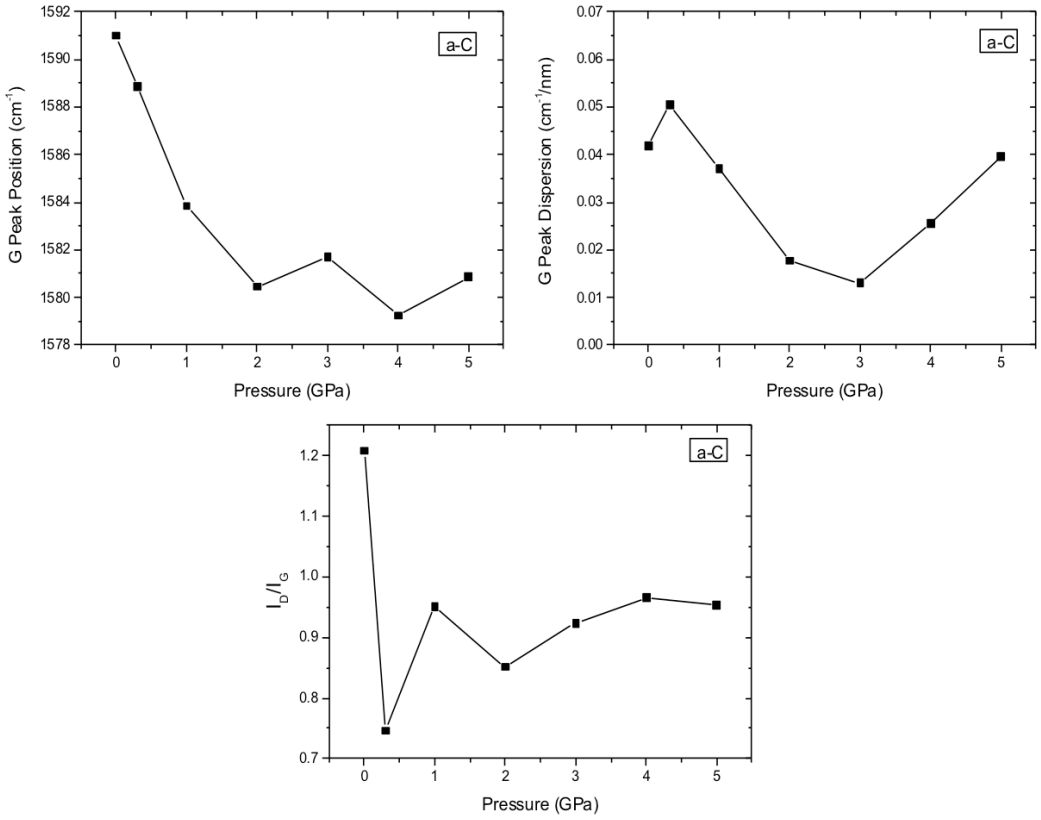

Figure 4-9. Raman data for pressed a-C films. G peak position generally decreases as pressure increases while I_D/I_G ratio generally increases with pressure. G peak dispersion is very low and implies the film is largely nano-graphitic.

Most significantly, the rough saturation of the G peak position as the pressure increases indicates that there is little if any conversion of sp^2 bonds to sp^3 at these pressure and temperature combinations. This is not particularly problematic unless higher resistivity films approaching that of diamond are desired.

4.1.6 Sulfur Doped Film Raman Results

As shown in Figure 4-10, the G peak position and dispersion show similar slight increases in the sp^2 bond disorder with pressure or dopant percent as the undoped films. The I_D/I_G ratio does increase with pressure for 5% and 10% doping

indicating that there is some increase in clustering and local ordering. The change in I_D/I_G ratio and the relative lack of fragility of the sulfur-doped films indicates that sulfur increases clustering, likely by vulcanization like crosslinking, with the carbon.

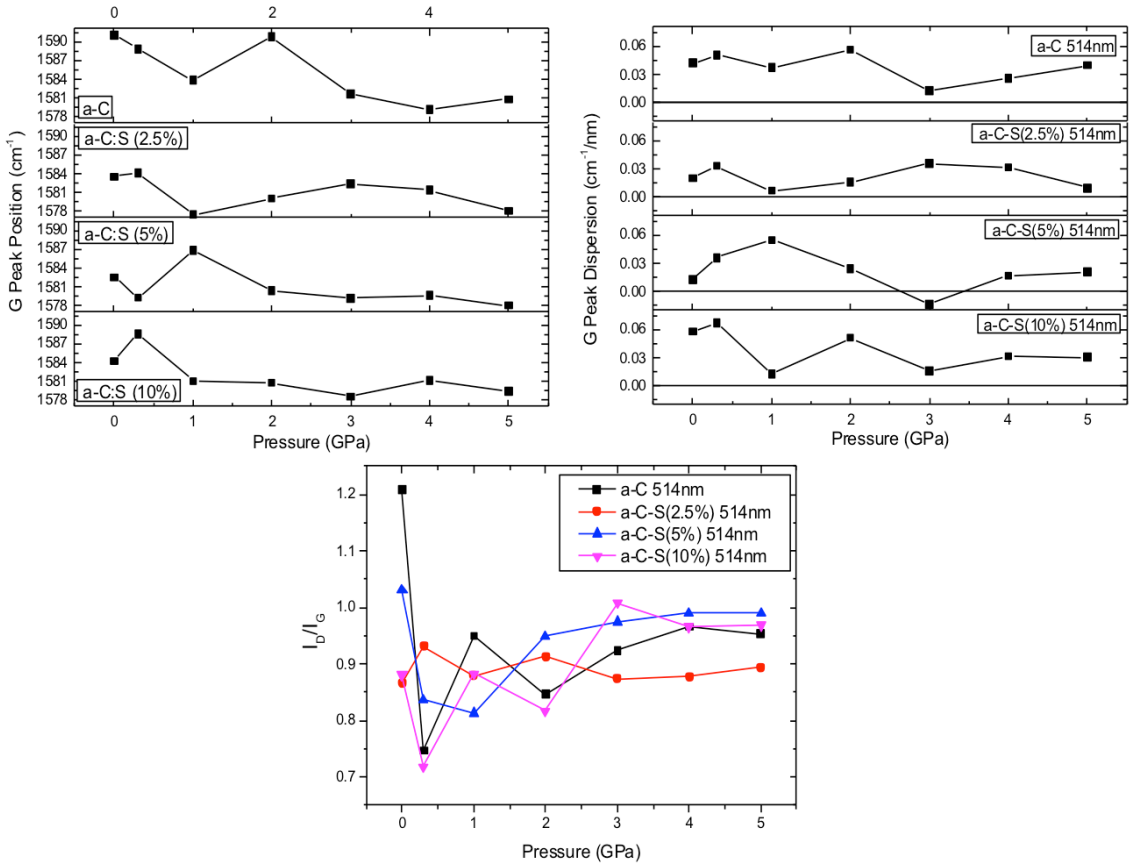

Figure 4-10. Raman data for sulfur-doped pressed a-C films. G peak position and G peak dispersion show similar changes with pressure as the undoped films and little dependence on dopant percent. I_D/I_G ratio increases with pressure for 5% and 10% doping levels.

4.1.7 Boron Doped Film Raman Results

As shown in Figure 4-11, the G peak position shows a general, slight increase with pressure and is higher than that of undoped a-C. This indicates the addition of boron stops the increase in disorder with pressure seen in undoped films. G peak

dispersion shows no significant change with pressure or dopant percent and remains very low as is typical in nanographitic films. I_D/I_G ratio shows no distinct trend with pressure or dopant percent. Significant I_D/I_G variation however likely indicates non-uniform clustering. Overall, the lack of significant change in the Raman spectra is not surprising in light of the observed fragility of the films.

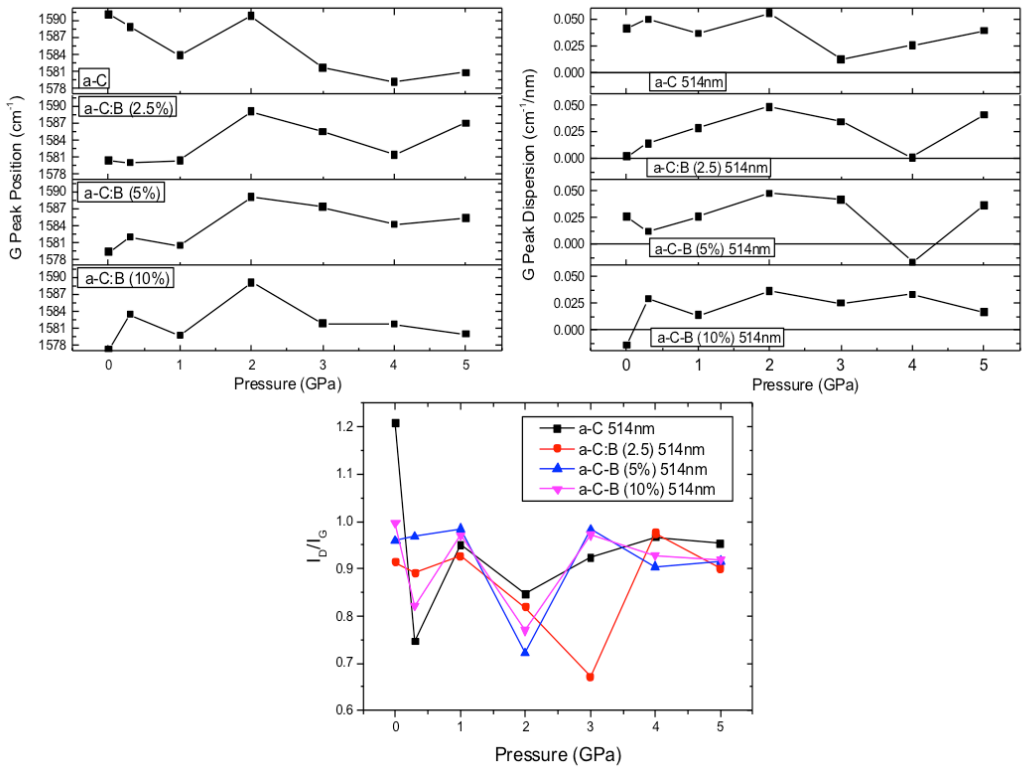

Figure 4-11. Raman data for boron doped pressed a-C films.

4.2. Resistivity Measurements

4.2.1 Introduction

Bulk resistivity (ρ) is a measure of how strongly a material opposes the flow of electric current and has units of Ω-m, or more commonly, Ω-cm for semiconductors. An accepted technique for determining the bulk resistivity is the

van der Pauw method. [47] In this method, a four-point probe, constant current source, and voltmeter are used on a thin film to determine the bulk and sheet resistivity.

The bulk resistivity of a film is related to the sheet resistivity such that

$$\rho = R_S d \qquad \text{(Equation 4-2)}$$

where R_s is the sheet resistivity in Ω/□ and d is the film thickness in cm. The sheet resistivity R_s is given by:

$$R_s = e^{\left(-\frac{\pi R_A}{R_S}\right)} + e^{\left(-\frac{\pi R_B}{R_S}\right)} = 1 \qquad \text{(Equation 4-3)}$$

where R_A and R_B are determined using the convention shown in Figure 4-12. [47] For more accurate measurements of R_A and R_B, additional measurements are taken as shown by Equation 4-4.

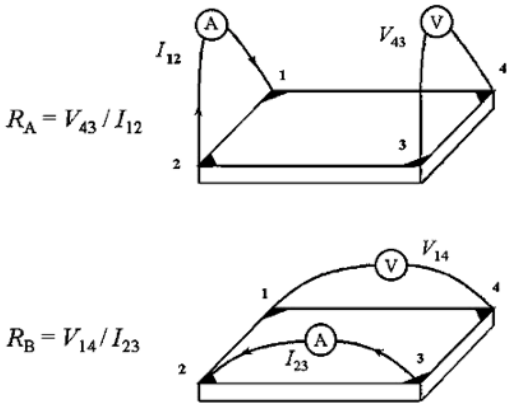

Figure 4-12. Schematic of voltage measurements given a constant current using the van der Pauw method. [47]

$$R_A = (R_{21,34} + R_{12,43} + R_{43,12} + R_{34,21})/4$$
$$R_B = (R_{32,41} + R_{23,14} + R_{14,23} + R_{41,32})/4 \quad \text{(Equation 4-4)}$$

4.2.2 Apparatus and Procedure

To conduct the resistivity measurements, the films were measured for thickness using a micrometer and then attached to glass microscope slide covers using Duco cement to reduce fracturing. Films are generally about (200±50)μm thick. The slide cover was then placed in the Ecopia SPCB-01 four-point probe test set shown in Figure 4-13. The Keithley 225 constant current source and 181 Nanovoltmeter (Figure 4-14) were warmed up for a minimum of one hour before taking measurements to allow the electronics to thermally stabilize. A known resistor was used to verify accuracy of the voltage measurements.

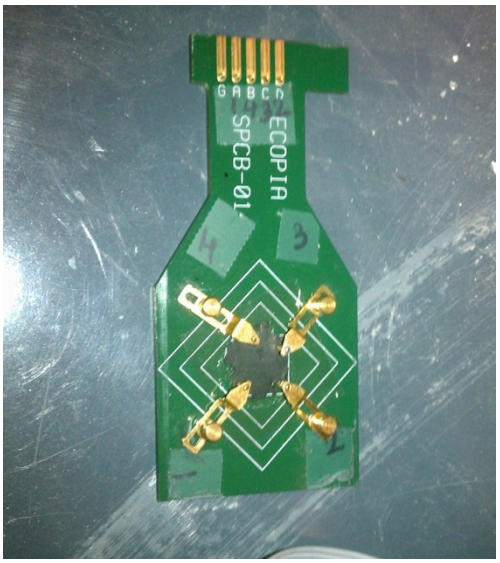

Figure 4-13. Ecopia SPCB-01 four point probe test set and pressed carbon film cemented to a glass microscope slide cover.

In order to minimize heating of the film and changing the resistivity, the current was set at 100μA, which typically resulted in voltage measurements on the

order of 1-5mV. The voltmeter was zeroed before each measurement after waiting for the voltage to stabilize after the previous measurement. A box was used to cover the films during testing to reduce the effects of photoconduction. Once the measurements were taken using the worksheet shown at Appendix A, an excel spreadsheet is used to iteratively calculate R_A, R_B, R_S, and ρ.

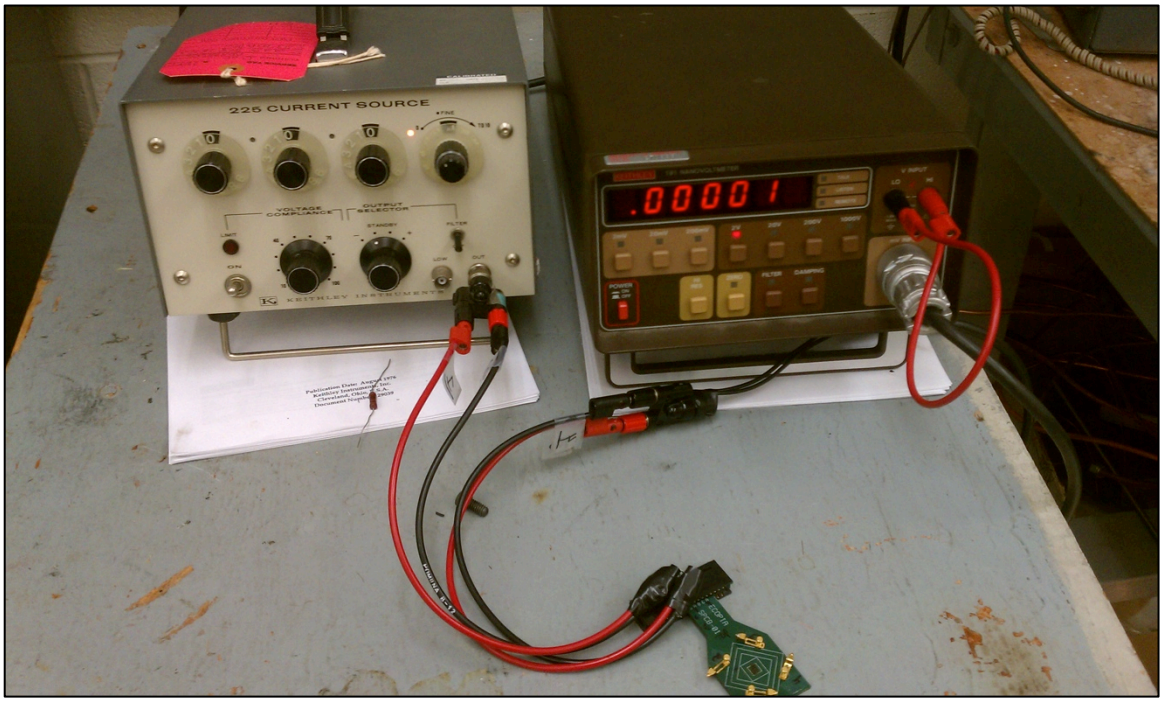

Figure 4-14. Resistivity test equipment. Keithley 225 constant current source, Keithley 181 Nanovoltmeter, and Ecopia SPCB-01 four point probe for van der Pauw measurements.

4.2.3 Results

4.2.4 Undoped Film Resistivity

The initial resistivity results for doped and undoped a-C films are shown in Figure 4-15. The resistivity of ~1 Ω-cm is in the semiconductor regime and similar to 10^{16} cm^{-3} doped 300K silicon. This resistivity is much less then that of diamond (10^{10} Ω-cm) and much higher than crystalline graphite (10^{-6} Ω-cm). For the

undoped a-C films, we see a monotonic ~30% decrease in resistivity through 4GPa before leveling off, within the uncertainty, at 5GPa. This decrease in resistivity occurs despite the slight increase in disorder shown in the Raman spectra likely due the increase in clustering shown in the I_D/I_G ratio. The increase in clusters provides additional tunneling/hopping locations for charge carriers and reduces resistivity.

4.2.5 Sulfur Doped Film Resistivity

We can clearly see that the addition of sulfur to the films reduces resistivity by a factor of 2-4X. As all six points (n=6) for each of the 2.5%, 5%, and 10% a-C:S films have a positive difference, there is ~99% confidence they are significantly different from the undoped baseline films per the Wilcoxon Signed Ranks Test(WSRT). [48] An example calculation for the WSRT is at Appendix B. We can also see that the a-C:S(5%) resistivity is ~30% less than that of the 2.5% and 10% sulfur films and significantly different with the same ~99% confidence.

The 2.5% sulfur line slope roughly mimics that of the undoped films in that it generally decreases as the pressure increases while the 5% and 10% lines are more constant. In doping amorphous films, there are opposing mechanisms of the dopant introducing defects that act as traps or introducing local order that can facilitate charge transport. It appears that the sulfur 5% doping level is the approximate inflection point that maximizes charge transport and is most effective for doping given these processing parameters.

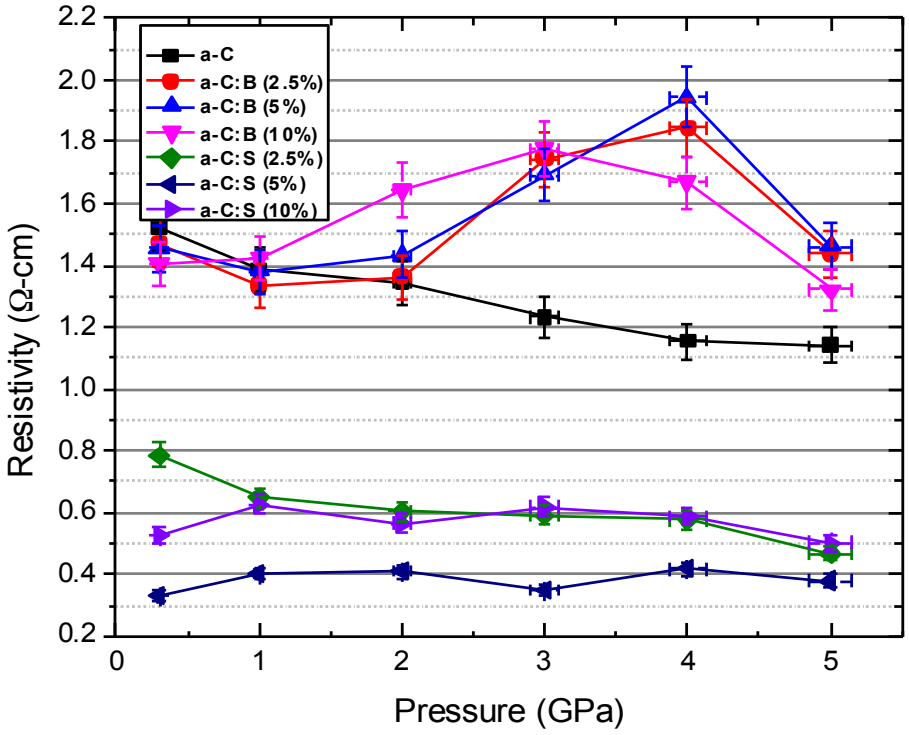

Figure 4-15. Resistivity results for a-C, a-C:S, and a-C:B.

There is a relative insensitivity to pressure for all sulfur-doped films compared to undoped films as shown by the surface graph in Figure 4-16. A second order polynomial provides a very good fit (adj R squared >.98) as shown in Table 4-B with doping percent approximately 5X more significant than pressure.

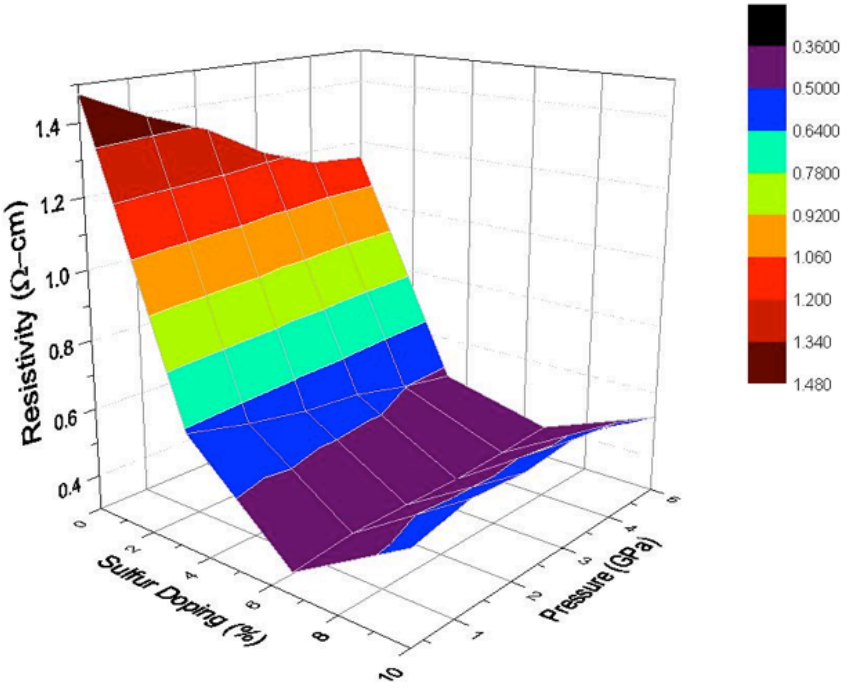

Figure 4-16. Surface graph of sulfur doped film resistivity highlights the much greater dependence on doping percent than pressure.

Table 4-B. Second order polynomial fit of sulfur doped film resistivity shown in Figure 4-16.

Model	Poly2D	
Equation	z=z0+a*x+b*y+c*x ^2+d*y^2+f*x*y;	
Reduced Chi-Sqr	0.00177	
Adj. R-Square	0.98659	
	Value	Standard Error
z0	1.44061	0.03382
a	-0.2987	0.00892
b	-0.05884	0.02251
c	0.021	7.73117E-4
d	-6.75969E-4	0.0039
f	0.00725	0.00144

4.2.6 Boron Doped Film Resistivity

While not as effective as changing the resistivity of the films as sulfur, boron doping provides a interesting case in that there is a significant pressure sensitivity and the resistivity profile is considerably different than the a-C film as shown in Figure 4-15. The 2.5% and 5% films initially start off less resistive than a-C at low pressures before spiking up by 25-40% at mid-level pressures and then returning to their approximate initial resistivity at 5GPa. The 10% doped film acts similarly but has a flatter profile.

In order to quantify statistically the likelihood that matched samples are significantly different, the WSRT was run in OriginPro on the doped samples as shown in Table 4-C. These results clearly highlight that the a-C:S films are significantly different from a-C at all pressures. The a-C:B films have lower significance levels primarily because of the similar resistivity at lower pressures. Assessing the films only at higher pressures would increase the significance of how different the films are.

Table 4-C. Wilcoxon signed ranks test results for differences in film resistivity.

Sample 1	Sample 2	Probability that statistically significant difference (higher is better)
a-C	a-C:B(2.5%)	>70%
a-C	a-C:B(5%)	>90%
a-C	a-C:B(10%)	>95%
a-C:B(2.5%)	a-C:B(5%)	>70%
a-C	a-C:S(2.5%)	>99%
a-C	a-C:S(5%)	>99%
a-C	a-C:S(10%)	>99%

Unlike the sulfur-doped films however, the boron-doped films do not cleanly fit a second order polynomial. As shown in Figure 4-17 and Table 4-D, the fit quality is very poor with an adjusted R squared of only 0.28 when the full range of pressures and doping percentages is used.

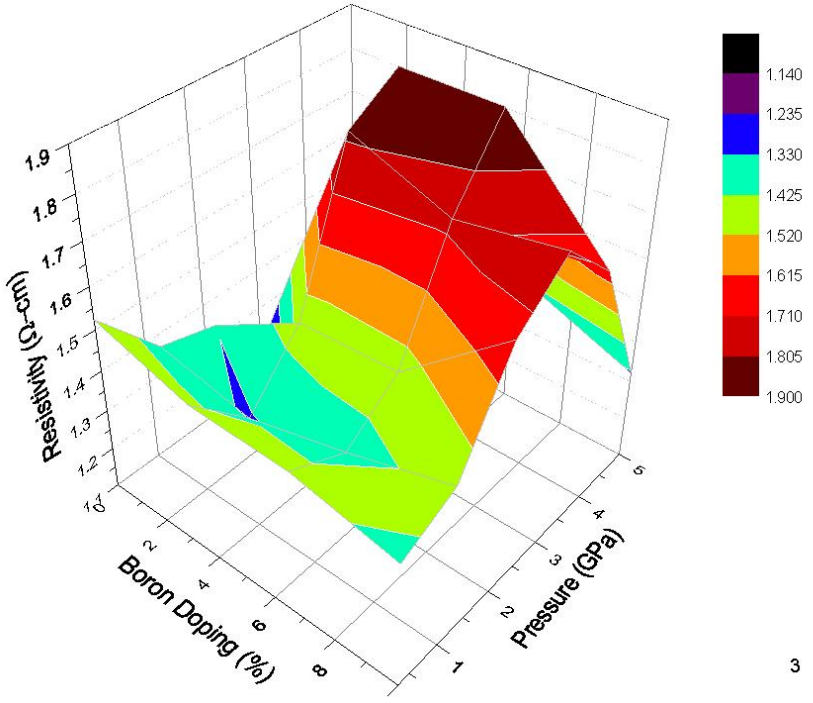

Figure 4-17. Surface resistivity graph of boron-doped films at all pressures and doping percentages.

Table 4-D. Fit data for the full range surface resistivity graph of the boron-doped films shown in Figure 4-17.

Model	Poly2D	
Equation	z=z0+a*x+b*y+c*x^2+d*y^2+f*x*y;	
Reduced Chi-Sqr	0.03369	
Adj. R-Square	0.28632	
	Value	Standard Error
z0	1.23653	0.14748
a	0.06916	0.0389
b	0.14009	0.09819
c	-0.0066	0.00337
d	-0.03163	0.017
f	0.00753	0.00626

Fitting only pressures >2GPa however improves the fit considerably and raises the adjusted R squared value to ~0.84.

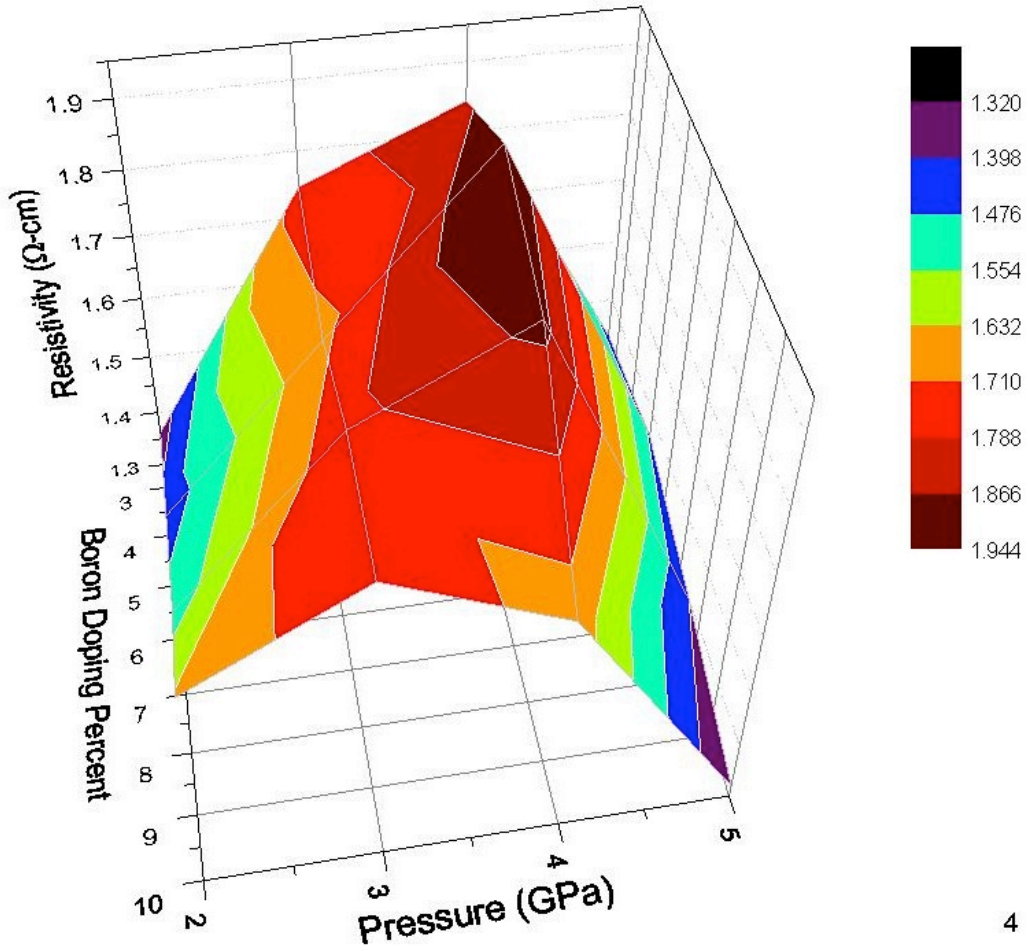

Figure 4-18. Surface resistivity graph of boron-doped films at all pressures and doping percentages.

Table 4-E. Fit data for the full range surface resistivity graph of the boron-doped films shown in Figure 4-18.

Model	Poly2D	
Equation	z=z0+a*x+b*y+c*x^2+d*y^2+f*x*y;	
Reduced Chi-Sqr	0.00642	
Adj. R-Square	0.84081	
	Value	Standard Error
z0	-0.73127	0.29092
a	0.10367	0.04649
b	1.3078	0.14697
c	-0.00292	0.00321
d	-0.1722	0.02004
f	-0.01895	0.00641

The model fit data in Table 4-E highlights that unlike the sulfur-doped films, the boron-doped films are much more strongly (~13X) dependent upon the pressure than the doping percent. Where sulfur had an inflection point at 5% doping level, boron films processed in this manner appear to be relatively insensitive to doping percent but have a local maximum inflection point for resistivity at 3-4GPa.

As there is no decrease in resistivity, it would appear that the boron atoms are not substitution doping or providing shallow acceptor levels in the energy gap. Increased resistivity and little change in the Raman spectra makes it likely that the boron atoms are agglomerating at grain boundaries and not changing the carbon-bonding network to any significant degree, resulting in a poor dopant.

4.3. Hall Effect Measurements

4.3.1 Introduction

The objective of the Hall effect measurement is to determine the sheet carrier concentration n_s and carrier mobility μ of a sample by measuring the Hall voltage V_H. [47] This measurement is conducted using the resistivity measurement equipment

with the addition of a magnet. Resistivity measurements are first taken as described earlier. As shown in Figure 4-19, the Hall voltage is then measured perpendicular to a constant current *I* and a constant magnetic field *B. B* is applied perpendicular to the plane of the sample. To measure the Hall voltage V_H, a current *I* is forced through opposing pairs of contacts as shown in Figure 4-20 and the Hall voltage V_H measured across the remaining pair of contacts. As shown in the worksheet at Appendix A, measurements are taken from each pair of contacts with both positive and negative polarity and magnetic field for a total of eight measurements. These V_H measurements are then summed. A useful byproduct of the Hall effect measurement is that when ΣV_H is positive, the majority carriers are holes and the material is p-type. If ΣV_H is negative, the majority carriers are electrons and the material is n-type.

Once V_H is acquired, the sheet carrier concentration n_s can be calculated:

$$n_s(cm^{-2}) = \frac{IB}{q\,\Sigma V_H} \qquad \text{(Equation 4-5)}$$

and the carrier mobility μ is then:

$$\mu(\frac{cm^2}{V \cdot s}) = \frac{1}{q n_s R_s} \qquad \text{(Equation 4-6)}$$

where R_s is the sheet resistivity from the resistivity measurement. [47]

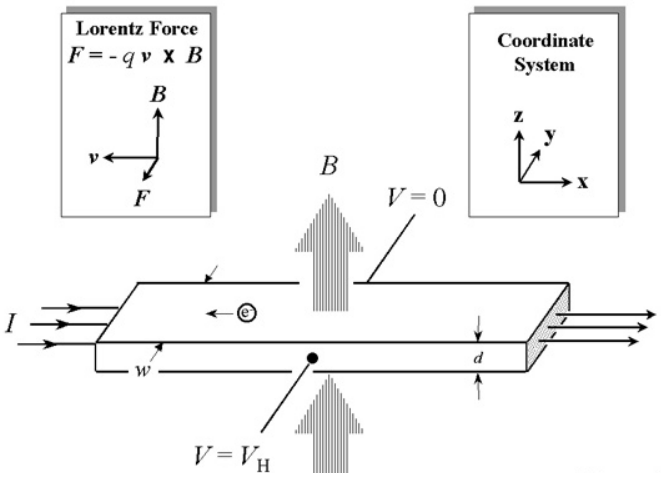

Figure 4-19 Principle of the Hall Effect.

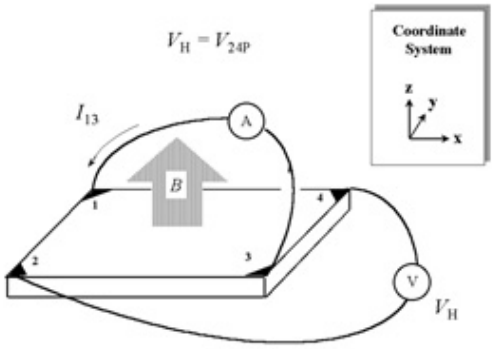

Figure 4-20. Measurement schematic for the Hall effect.

4.3.2 Apparatus and Procedure

The majority of the apparatus is as previously described in the resistivity section with the exception of the GMW 5403 electromagnet and sample holder shown in Figure 4-21. After conducting resistivity measurements as previously described, the test set and film is placed in the electromagnet and the magnet voltage brought slowly up to 20V. Water cooling is used to ensure a stable magnet temperature. Once the voltage stabilizes, a gaussmeter is used to determine the magnetic field strength at the film location and then Hall effect measurements are

taken similar to the procedures for resistivity. After the first four measurements, the test set is rotated 180° to change the direction of the B field through the film and then the other four measurements taken. Once complete, the magnet power supply is slowly decreased to zero and then the film removed. The data is then entered into a Excel spreadsheet that calculates V_H, n_s, *and* μ. The data is then imported into OriginPro for graphing and statistical analysis.

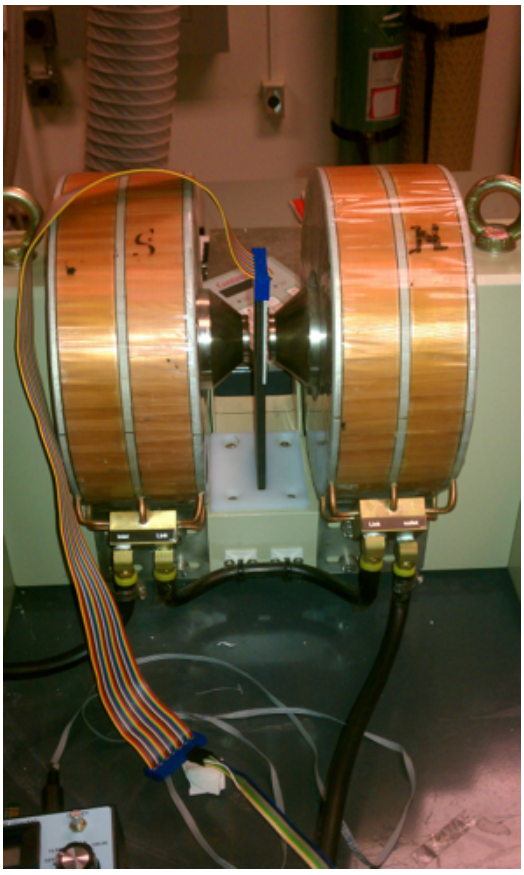

Figure 4-21. GMW 5403 electromagnet and van der Pauw test set holder.

4.3.3 Hall Voltage Results

The first calculated Hall effect results are the Hall voltages, which can be used to determine majority carrier type. Note that during this second set of

measurements, several films fractured to the point they could not be measured and therefore are missing in the following charts. These films were not replaced to ensure that there was not an additional film age related variable in the results.

The consolidated data for undoped, and sulfur and boron doped films is shown in Figure 4-22. The data points that are available for the undoped films show the expected p-type nature. Not surprisingly considering the Raman and resistivity data, it appears that the addition of boron to the carbon films had little to no effect as a dopant. The addition of sulfur however changed the Hall voltages to negative, indicating a conversion to an n-type film with electron majority carriers. Because there are too many missing data points however, it is premature to draw any specific conclusions about the relationship between doping percent and Hall voltage.

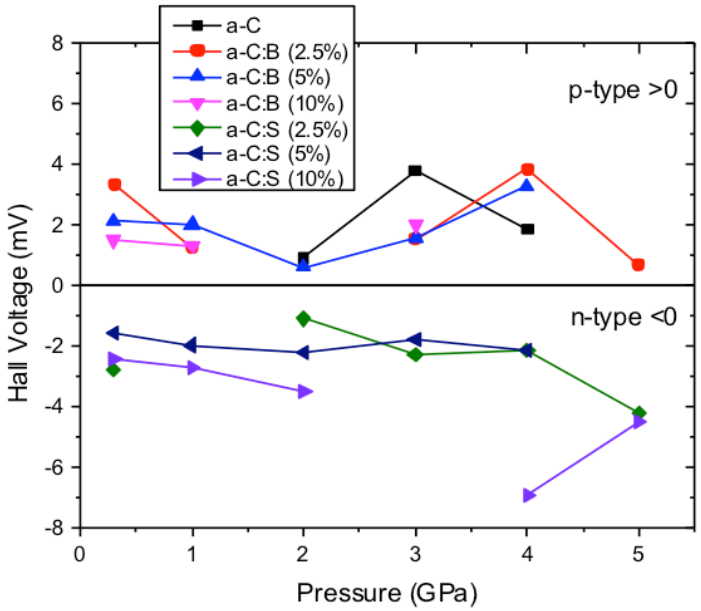

Figure 4-22. Hall voltages highlighting p-type behavior for a-C and boron doped films and n-type behavior for sulfur doped films.

4.3.4 Carrier Concentration Results

Despite the change in Hall voltage indicating n-type doping using sulfur, the carrier concentrations shown in Figure 4-23 do not vary significantly from that of the undoped films and there is no clear relationship between doping percent and the concentration. Carrier concentrations are on the order of 10^{19} cm^{-3}. Further work is needed to establish a process that can control the doping parameters. Similarly inconclusive results are seen in Figure 4-24 for boron-doped films.

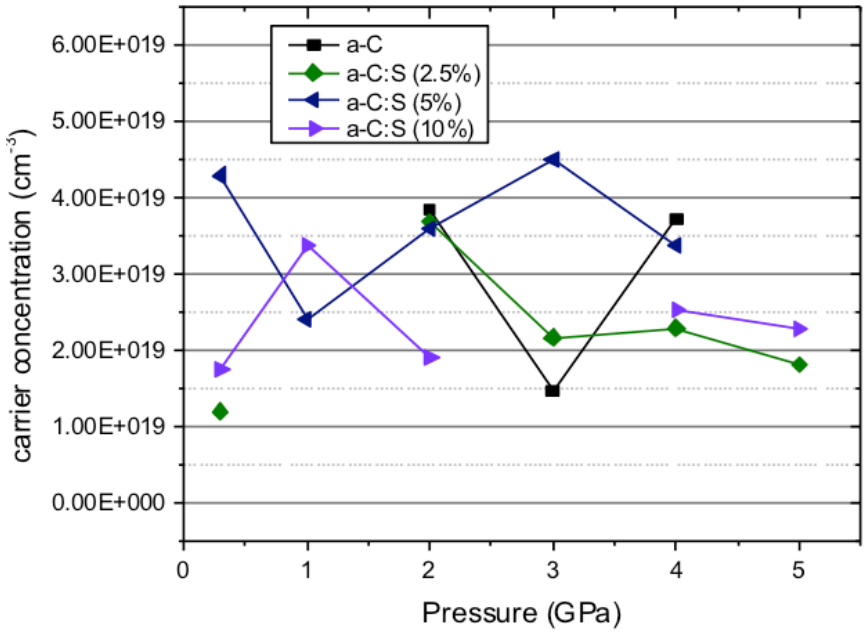

Figure 4-23. Carrier concentration for undoped and sulfur doped films.

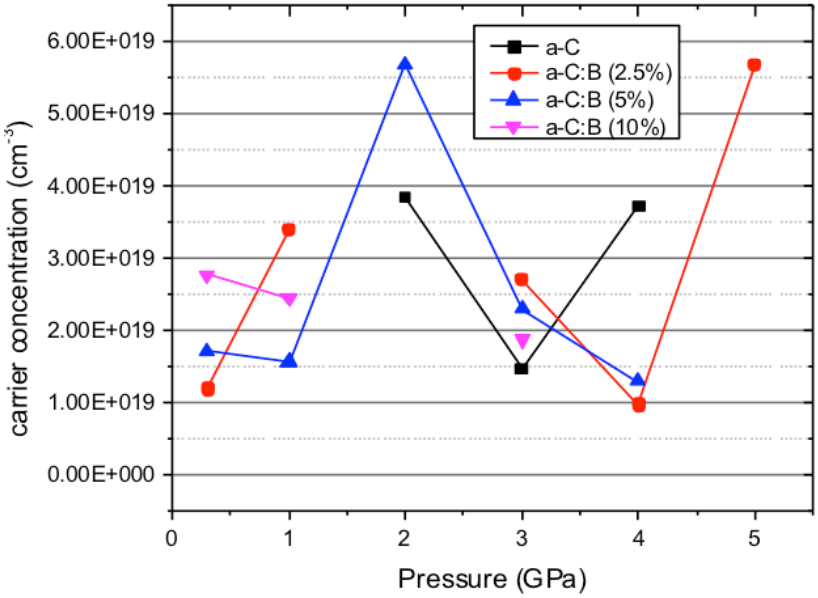

Figure 4-24. Carrier concentration for undoped and boron doped films.

4.3.5 Carrier Mobility Results

The mobilities in the sulfur-doped films shown in Figure 4-25 and boron-doped films in Figure 4-26 do not show any clear trend with doping percent. Mobility is <1 cm^2/V-s which is of the order of amorphous silicon but considerably less than crystalline silicon which has a typical electron mobility of >1300 cm^2/V-s at room temperature. We do see that there is a slight increase in the average mobility from 0.155 cm^2/V-s in the undoped films to 0.211 cm^2/V-s in the boron doped films. The sulfur films have an average mobility of 0.409 cm^2/V-s which is reasonable as it is typical for electron mobilities to be higher than hole mobilities in most semiconductors.

Table 4-F. Aggregate mobility data for undoped and doped films

	Undoped	Boron Doped	Sulfur Doped
Mobility Average (cm^2/V-s)	0.155	0.211	0.409
Standard Deviation	0.056	0.100	0.143

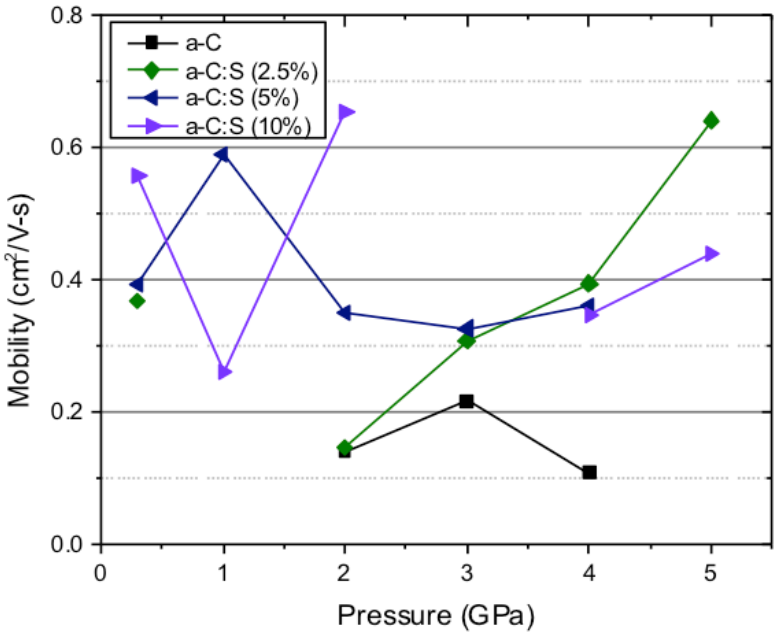

Figure 4-25. Mobility data for undoped and sulfur-doped films.

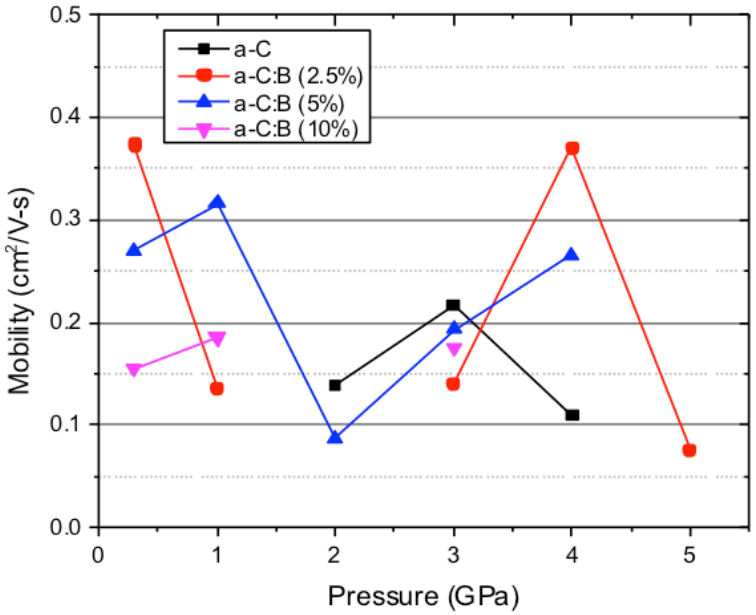

Figure 4-26. Mobility data for undoped and boron-doped films.

5. PN Junction/PIN Device Fabrication and Characterization

5.1. PN Junction and PIN Diodes Introduction

Semiconducting materials are essential to solid-state devices. The PN junction diode is a common electronic device fabricated by combining p-type and n-type semiconducting regions. The mechanical and electronic properties of the materials in these regions are dictate device performance.

There are two key principles that occur in a PN junction. The first is that the Fermi energies are approximately at the donor level for n-type materials and at the acceptor level for p-type materials. Second, when the p- and n-type materials are placed together in intimate contact, equilibrium requires charge to transfer until the Fermi energies equalize in both materials. As shown in Figure 5-1, the excess mobile holes from the p-type material diffuse to the n-type, which has a much lower hole concentration until equilibrium is established. [49] Similarly, the majority electrons from the n-type diffuse to the p-type side. The remaining fixed charges generate an electric field that creates a drift current in opposition to the diffusion current. An unbiased PN junction will reach an equilibrium point where the drift and diffusion currents exactly balance out leaving a “depletion region” with few mobile carriers.

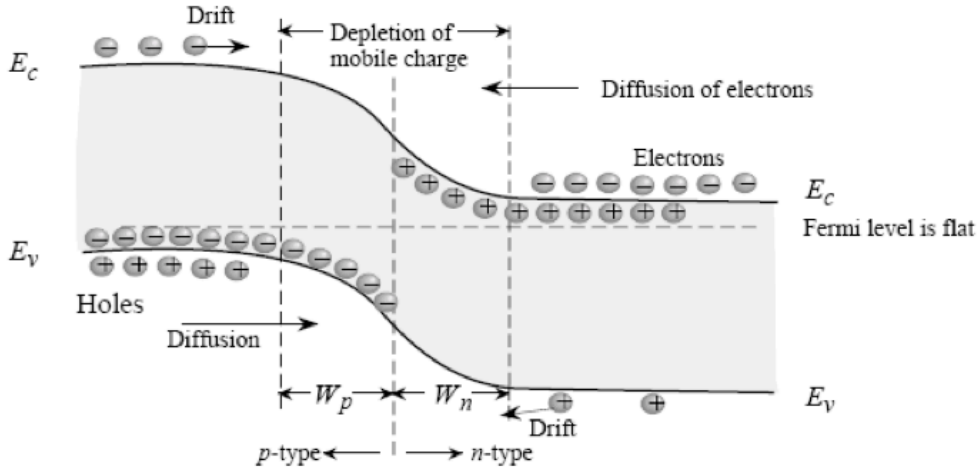

Figure 5-1. Mating of p- and n-type materials in an unbiased PN junction results in the bands bending until the Fermi level is equal on both sides of the junction. [49]

PN junctions have many applications that take advantage of their properties when biased under either a positive or negative voltage. For voltaic devices however, the desire is to produce power from an external energy source using an unbiased PN junction. As shown in Figure 5-2, when an electron-hole pair (EHP) is created in the depletion region of the PN junction, the electric field may separate the charges prior to them recombining resulting in current flow if connected in a closed circuit. EHP created outside the depletion region may also contribute to the current if they do not combine immediately and diffuse away from each other. In a photovoltaic, one EHP is generally created for every photon that exceeds the band gap of the material. In an alpha or betavoltaic, thousands to millions of EHP are created as the ionized particle traverses the material. Unfortunately, the large amount of energy deposited over a short distance in the material can cause significant damage to the semiconductor device and change it's electronic and

material properties, particularly if based on a crystalline structure. Radiation damage will be discussed further in chapter 6.

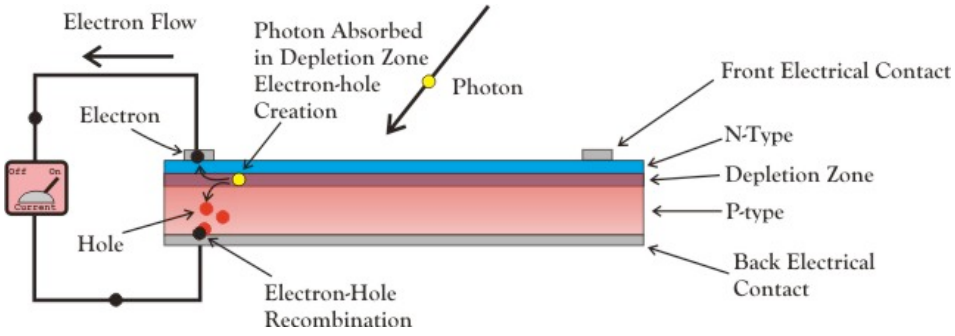

Figure 5-2. Schematic of a photovoltaic device. Radioisotope voltaics use radio-active decay products instead of photons to produce electron hole pairs. [50]

A PIN diode is similar to a PN junction except that it has a relatively wide intrinsic region between the p- and n-type materials. The PIN diode can act differently than a PN junction in some types of devices but for the voltaic device aspect of this research, the primary effect of the intrinsic region is to widen the depletion region considerably, allowing a larger area for photons, or alpha and beta particles to efficiently create EHPs that form current and power.

5.2. Thermomechanical PN Junction and PIN Diode Fabrication Apparatus and Procedure

PN junctions and PIN devices were fabricated using two different techniques. The first technique utilized largely the same procedures for fabricating the individual films as described in chapter 3. The difference being that in order to minimize powder mixing and fabricate a relatively abrupt junction, the p- and n-type films were grown separately and then pressed together for 30 minutes at 109C and 300MPa. In order to assess the range of doping percentages and pressures, a

fractional factorial 2^{4-1} design with four centerpoint runs experimental design as shown in Table 5-A was used. The measured response was a binary pass/fail on whether the junction displayed rectification when characterized.

A total of six PN junctions were fabricated using this technique before the decision was made to attempt to fabricate PIN diodes due to lack of positive results as discussed later. Runs 1-3 of the below design were used for PIN diodes with the addition of 2GPa undoped films as the intrinsic layers. The individual films were stacked vertically on separate Ni substrates and pressed as shown in Table 5-A. The individual films were then pressed together at 1GPa, 109°C for 30 minutes.

Table 5-A. 2^{4-1} fractional factorial PN junction fabrication experimental design with four centerpoint runs.

StdOrder	RunOrder	CenterPt	Doping % (B)	Doping % (S)	Pressure (B)	Pressure (S)
8	1	1	10	10	5	5
11	2	0	5	5	3	3
1	3	1	2.5	2.5	0.3	0.3
5	4	1	2.5	2.5	5	5
12	5	0	5	5	1	1
4	6	1	10	10	0.3	0.3
2	7	1	10	2.5	0.3	5
7	8	1	2.5	10	5	0.3
6	9	1	10	2.5	5	0.3
9	10	0	5	5	2	2
3	11	1	2.5	10	0.3	5
10	12	0	5	5	4	4

5.3. Plasma Enhanced Chemical Vapor Deposition (PECVD) Apparatus.

The second PN junction and PIN device fabrication technique that was tried was to use a plasma enhanced chemical vapor deposition reactor (PECVD) to deposit known p- and n-type boron carbides onto carbon films.

The plasma enhanced chemical vapor deposition (PECVD) system consists of 4 major assemblies as shown from left to right in Figure 5-3 and Figure 5-4: the electronics package; gas flow and precursor assembly; reactor chamber; and vacuum system.

The electronics package consists of radiofrequency (RF) plasma generation, temperature control, vacuum monitoring, and turbo pump control. RF plasma is generated inside the reactor by a 13.56MHz RF generator with forward and reverse wattmeters.

There are four temperature controllers in the electronics package. One is for the argon supply line, two are for the precursor lines, and one is for the substrate heater in the reactor. The substrate temperature controller is a Brand-Gaus Model 611 Profiling Temperature Controller, which allows programming of cool-down or heat-up profiles. The other three temperature controllers are Brand-Gaus Model 411's, which do not have programmable profiles. Type K thermocouples are used.

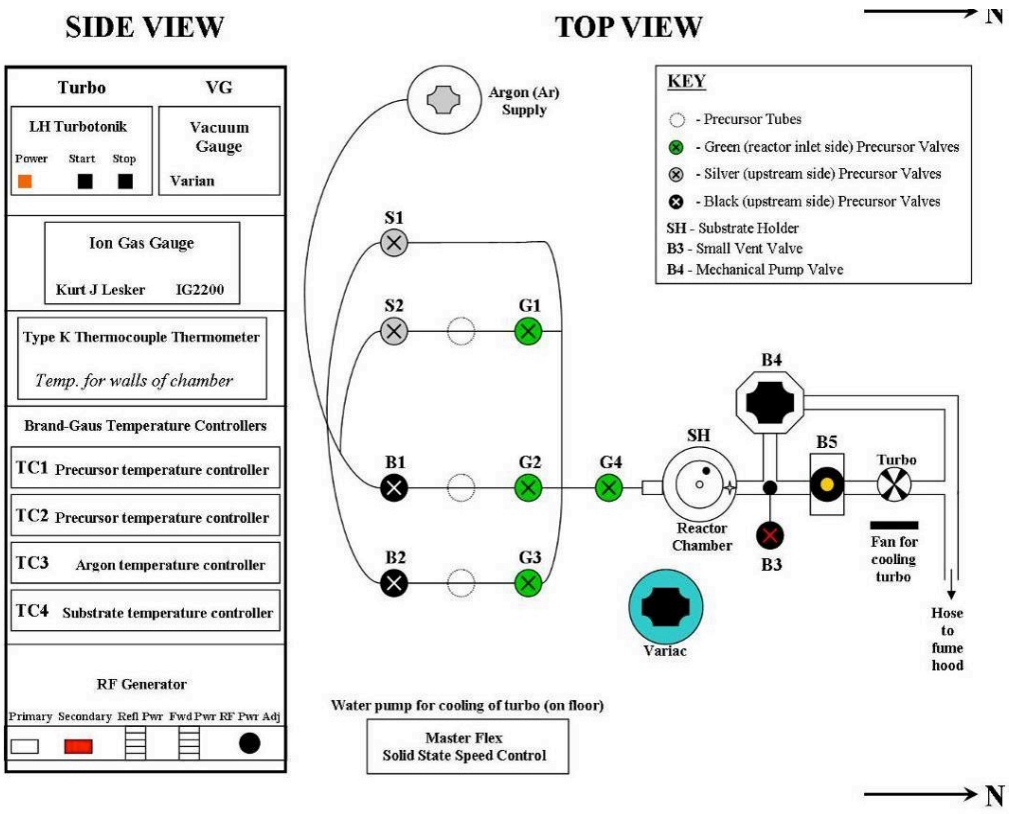

Figure 5-3. Schematic of the four major assemblies of the PECVD reactor system. From left to right: electronics package; gas flow and precursor assembly; reactor chamber; and vacuum system.

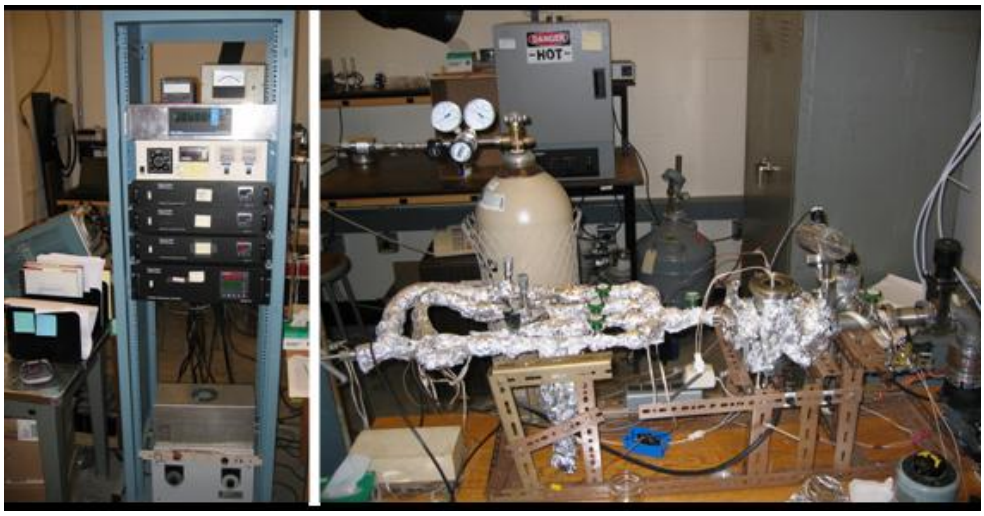

Figure 5-4. Split view picture of PECVD reactor assembly..

Vacuum monitoring consists of a Varian 802-A thermocouple vacuum gauge using a Lesker 4 pin thermocouple placed on the back of the reactor. A Leybold Vacuum Inc., Turbotronik NT 50 turbo pump controller controls the turbo pump.

The gas flow and precursor assembly controls the argon and precursor flow into the reactor. 99.9% ultra high purity argon from Linweld, Inc. is used as a carrier gas and is regulated to ~20 psi. A 0.003-micron Aeronex Model SS-35-KF-I-4R inert gas purifier further purifies the argon. The two precursors are stored in glass vials with stainless steel conflat flanges as shown in Figure 5-5.

Figure 5-5. Precursor glass vial with stainless steel conflat flanges and Swagelok fittings. Not shown is the thermocouple, heating tape, or insulating aluminum foil.

The individual vials are filled with orthocarborane (p-type) and metacarborane (n-type), which sublime well near room temperature. Each vial has a taped-on type-K thermocouple, is wrapped in heating tape, and covered in aluminum foil in order to maintain temperature control using the Brand-Gaus 411 temperature controllers. Swagelok stop valves are located on the reactor side of each vial. Swagelok and Whitey needle metering valves are located on the argon side in order to control the partial pressure of the precursor into the reactor. Precursor flow into the reactor is controlled by a combination of precursor temperature and argon carrier gas flow rate. All connecting tubing is stainless steel

and wrapped with the same heating tape as the corresponding precursor vial as well as aluminum foil to keep precursor gases sublimed until they reach the reactor.

The reactor consists of a 3" four-way stainless steel cross with quick flanges using Viton o-rings as schematically shown in Figure 5-6 and Figure 5-7. The substrate holder in inserted from the top. The cross has a glass view port to visually verify a plasma. The substrate holder is a 2.75" wide flat aluminum disc 0.25 inch thick at the end of a steel rod as shown in Figure 5-8.

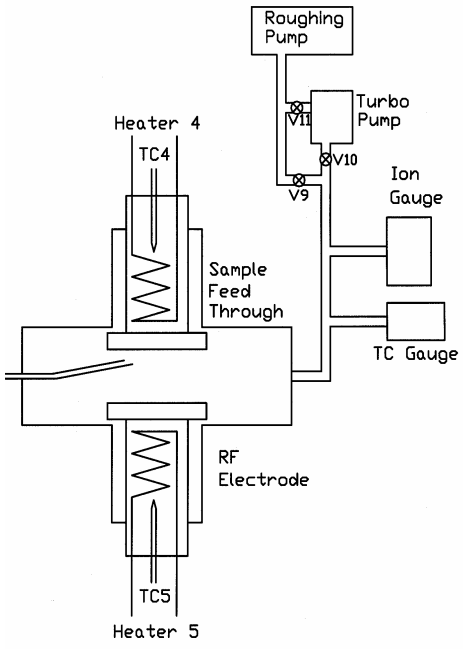

Figure 5-6. Schematic view of the plasma enhanced chemical vapor deposition reactor chamber.

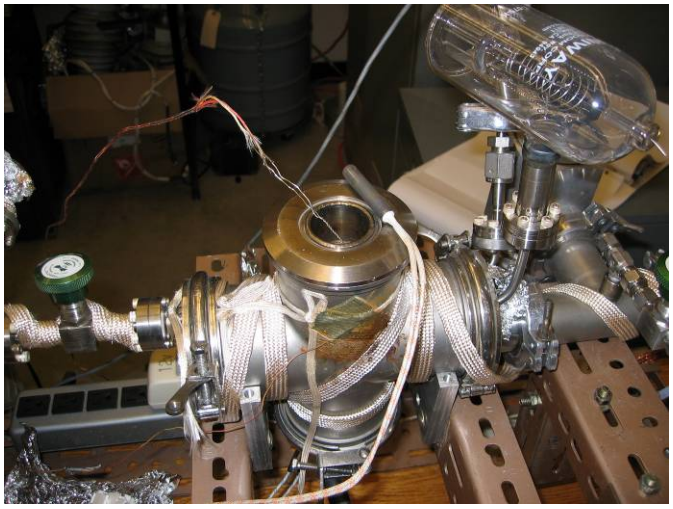

Figure 5-7. Reactor chamber made of a 4-way 3" cross using quick flanges. Precursors enter from left and vacuum pumps connect from the right. The RF plasma electrode is installed in the bottom flange. The top flange is removed to install substrates. Shown on the substrate holder is the substrate cartridge heater and thermocouple wire.

Figure 5-8. Substrate holder (top reactor flange). Shown is an aluminum mask and one carbon film.

The substrate holder is drilled down the center to allow the use of a 400W cartridge heater and type-K thermocouple controlled by the Brand-Gaus Model 611 Temperature Controller. The bottom flange is similar to the top flange as it has a steel tube with an aluminum disk at the end. The flange is connected to the RF plasma generator and the aluminum disk acts as the electrode. The heating tapes shown on the reactor are used to bake out the reactor between growing sessions.

The vacuum system utilizes a turbo pump in parallel with a mechanical roughing pump. The Edwards Model E2M2 roughing pump reduces the system pressure to ~1 mTorr. The Leybold Turbovac 50 turbo pump is capable of pumping to ~1 μTorr.

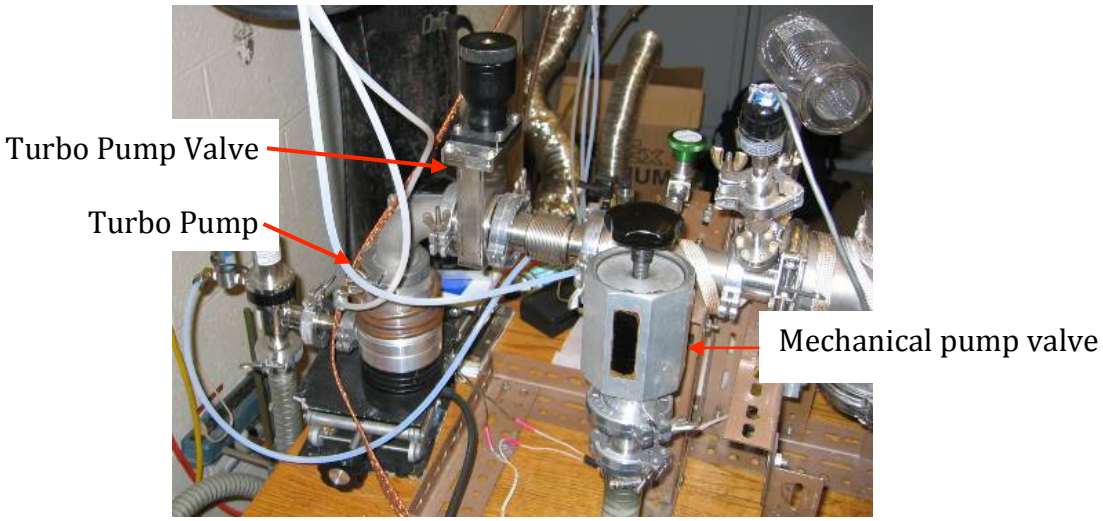

Figure 5-9. Vacuum pumping system. Separate valves can isolate the reactor from the mechanical pump (on floor) or turbo pump (at left on stand).

Both pumps are connected to the reactor as shown in Figure 5-9 but are isolated from each other by manual gate valves. The turbo pump exhausts into the mechanical pump inlet while the mechanical pump exhausts into a fume hood. An

accessory fan is used to cool the turbo pump. A molecular sieve trap at the inlet to the mechanical pump protects the pump oil from impurities and keeps pump oil out of the reactor and turbo pump. Regular pump ballasting and reactor bake outs are necessary to keep pressures low.

5.4. PECVD PN Junction and PIN Device Procedure

The detailed procedures for PECVD are found at Appendix C. In general, PECVD uses a radiofrequency plasma generator to ionize precursor atoms in a vacuum, which are then attracted to a substrate target on an electrode. This technique is roughly analogous to ion implantation used to dope many types of semiconductors. There are many variables to include precursor molecule type and temperature (vapor pressure), plasma power, substrate temperature, deposition time, substrate bias, and the substrate target material. In this research, well-established procedures from the Brand Group for boron carbide deposition were utilized as a baseline.

The concept for the PN junctions was to deposit n-type boron carbide using metacarborane onto a presumably p-type boron-doped thermomechanically processed carbon film. Orthocarborane, a p-type boron carbide precursor, was deposited on sulfur doped carbon films.

For the PIN devices, undoped and “compensated” carbon films were the substrate with orthocarborane deposited on one side with metacarborane deposited on the other side. The compensated films were a 50% mix of 10% boron and sulfur doped powder. The rationale was the compensated films were likely close to a

intrinsic film but may be able to take advantage of the apparent sulfur crosslinking that made the sulfur films less brittle. As a PIN device is more ideal for alpha or beta voltaics than a PN junction due to the larger depletion region, the limited time available to grow films was largely devoted to PIN devices. A maximum of one variable was changed for each growth to accurately track effects of changes. In order to minimize variables the deposition time was set at 60 minutes and partial pressure at 75mTorr for both orthocarborane and metacarborane. Argon temperature was fixed at 60°C and 150mTorr. Growth parameters are described below in Table 5-B with results discussed later.

Table 5-B. PN junction, PIN device PECVD growth parameters

Device	Substrate	T_{meta} (°C)	T_{ortho} (°C)	T_{sub} (°C)	RF Power (W)	Comment
PN #1	a-C:B(5%) 4GPa	55	N/A	350	25	n-type BC on p-type C
PN #2	a-C:S(5%) 3GPa	N/A	55	350	25	p-type BC on n-type C
PIN #1	a-C 2GPa	55	N/A	350	25	Baseline PIN parameters
PIN #2	a-C 2GPa	55	N/A	350	25	Repeat PIN #1; better pressure control
PIN #3	a-C 2GPa	55	N/A	330	25	Reduced $T_{substrate}$; meta pressure high during deposition
PIN #4	a-C 2GPa	45	55	330	25	Lowered T_{meta}; low ortho pressure during deposition
PIN #5	a-C 2GPa	45	70	330	25	Raised T_{ortho}
PIN #6	Compensated	55	70	250	25	Reduced $T_{substrate}$
PIN #7	Compensated	55	70	150	25	Reduced $T_{substrate}$
PIN #8	Compensated	55	70	30	25	Reduced $T_{substrate}$
PIN #9	Compensated	55	70	150	15	Raised $T_{substrate}$;
PIN #10	Compensated	55	70	150	15	Repeat PIN #9

5.5. Characterization Apparatus and Procedure

Current-voltage (I-V) measurements of the films were conducted using a Keithley 6517A Electrometer and Ecopia SPCB-01 four point probe as shown in Figure 5-10. The electrometer is connected to a laptop computer via a IEEE-488 General Purpose Interface Bus (GPIB) cable and card. The electrometer is controlled by Labview software, which has options for starting and ending voltage, voltage step size, voltage hold time, and a two way switch.

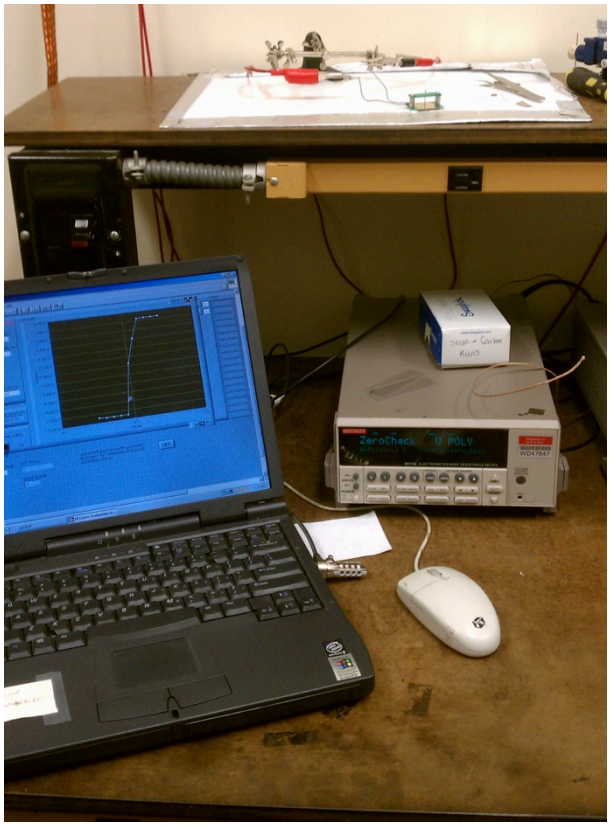

Figure 5-10. I-V curve measurement system consisting of a laptop running Labview software which controls a Keithley 6517A Electrometer over a IEEE-488 interface.

All testing of potential diodes is done in the dark under a box that is covered in aluminum foil connected to a common ground. The Labview software was typically configured to start running from -1 volt to 1 volt in 0.01 volt steps with a

voltage hold time of 250ms. The software displays the resulting I-V curve on the screen, which allows instant assessment of general resistivity of the film and the possibility of diode rectification. The data was then saved to a text file for later graphing. As the current through the devices saturated the ammeter, the voltages were decreased to -.1V to .1V before the saturation disappeared. The ideal I-V curve in Figure 5-11 shows current growth is exponential under forward bias and nearly zero and linear under reverse bias. [49] Reverse breakdown occurs under large reverse bias when electrons have enough kinetic energy to ionize additional electrons as they move through the material.

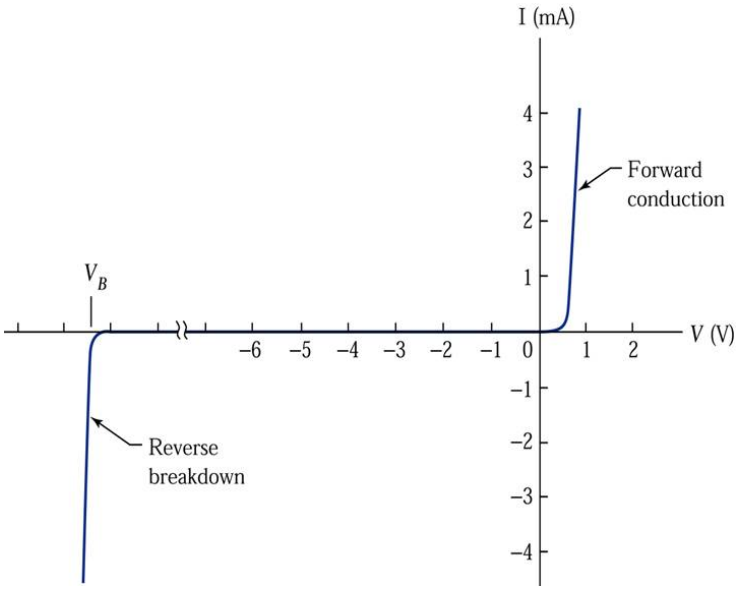

Figure 5-11. Current-Voltage (I-V) characteristics of a nearly ideal, real PN junction diode where forward bias occurs for V>0. [49]

5.6. PN Junction and PIN Device Results

5.6.1 Thermomechanically Processed PN Junction and PIN Devices

Pressing two separate boron and sulfur doped films together into a PN junction or PIN device was challenging and requires further process development. The films

were inconsistent in thickness from edge to center if pressed at <1GPa but had significant fracturing if pressed >1GPa. The open sided metal push plates work reasonably well for individual films but does not control the films well enough when stacked. The next step is likely to construct a cylinder with two compression pistons to control the size of the film given an exact amount of powder.

One of the six PN junctions and two of the three PIN devices were damaged prior to or during measurement due to their brittleness. None of the five remaining PN junctions or one PIN device displayed rectifying behavior and appeared to behave as resistors as shown in Figure 5-12. We can determine the resistance of the films from the slope of the I-V curves with the results shown in Table 5-C. Resistivity could not be accurately measured due to the significant thickness variations. Resistivity measurements would also be suspect as the films were relatively thicker compared to their diameter than is acceptable for the van der Pauw technique.

Table 5-C. Resistance of thermomechanically processed PN, PIN devices

Device	Resistance (Ω)
PN #2	24
PN #3	19
PN #4	50
PN #5	24
PN #6	18
PIN #1	15

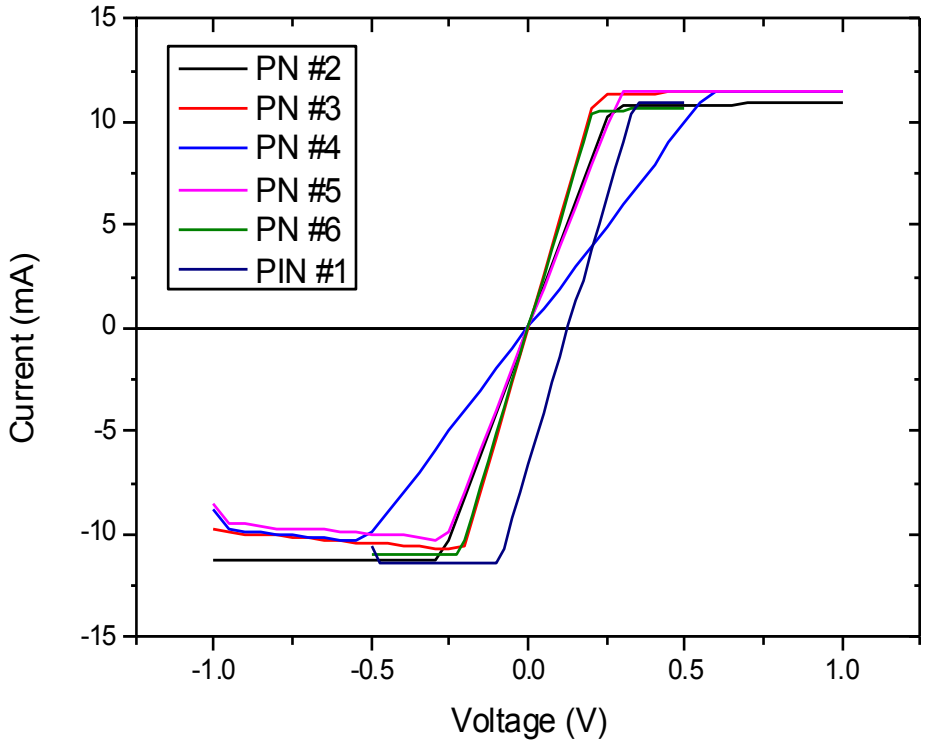

Figure 5-12. I-V curves of thermomechanically processed PN and PIN devices displaying lack of rectification and only resistor like behavior.

5.6.2 PECVD Processed PN Junction and PIN Devices

Only one each PN and PIN device survived PECVD fabrication and was able to be evaluated for junction characteristics. As shown in Figure 5-13, the two devices failed to show rectifying junction behavior and appear as resistors.

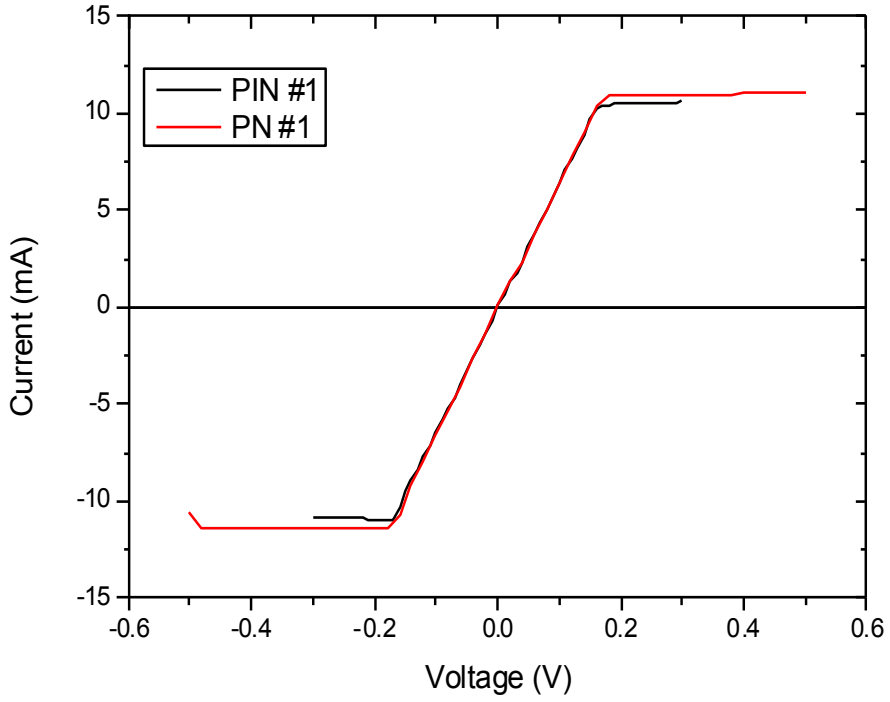

Figure 5-13. I-V curves for PECVD processed PN and PIN devices showing lack of rectifying characteristics and only resistor like behavior.

The fabrication results, by film, are summarized in Table 5-D. In general, PECVD is an energetic process and the brittle carbon films are easily damaged. Only 2 of 12 films survived both metacarborane and orthocarborane deposition. It appears a substrate temperature of 150°C is the minimum needed to enable BC atoms to stick to the carbon film. Higher substrate temperatures however appeared to increase the brittleness of the films.

Plasma power is likely a key variable that needs to be minimized to the minimum necessary to deposit a BC layer. Total and partial pressures were fixed through this effort but it is possible that reducing the pressure could enhance the

survivability of the films. A more detailed study of the effects of varying parameters is needed to determine if this procedure is even viable. At a minimum, a factorial design using plasma power, total pressure, $T_{substrate}$, and carbon film type is needed to assess the factors. Given the right equipment, ion implantation may be more suitable than this technique.

Table 5-D. Results for PECVD fabricated PN and PIN devices

Device	Substrate	Results
PN #1	a-C:B(5%) 4GPa	No obvious BC layer on C film; resistor behavior of 18Ω
PN #2	a-C:S(5%) 3GPa	Film damaged upon removal; appeared to have BC layer on fragments
PIN #1	a-C 2GPa	~800nm BC layer on both sides; Resistor 16Ω
PIN #2	a-C 2GPa	Film appears swollen and broke during removal after initial meta deposition
PIN #3	a-C 2GPa	Film fragmented and fell off substrate during meta deposition; find meta vapor pressure high as heat soaked after multiple depositions; reduced T to 45°C
PIN #4	a-C 2GPa	Film had BC layer after meta deposition but fragmented during ortho deposition; low ortho pressures during deposition
PIN #5	a-C 2GPa	Film had thin (~400nm) BC layer after both meta and ortho depositions; brittle however and broke during I-V curve measurement
PIN #6	Compensated	Film fragmented during meta deposition; tried thinner, smaller Al foil mask to reduce likelihood of film fragmenting
PIN #7	Compensated	Film fragmented during initial meta deposition
PIN #8	Compensated	Film survived initial meta deposition on lower, unheated electrode but had no noticeable BC layer on mask or C film; fragmented after repeating meta deposition on top unheated electrode and had no noticeable BC layer on mask or fragments
PIN #9	Compensated	Film had ~1μm BC layer from meta deposition; fragmented during ortho deposition
PIN #10	Compensated	Film fragmented during meta deposition

6. Effects of Radiation

6.1. Radiation Damage

One of the primary long-term issues with voltaic devices is the degradation of the semiconductor electronic and material properties due to exposure to radiation. In general, radiation can cause damage due to ionizing and nonionizing energy loss.

Ionizing energy loss occurs when a charged particle or photon pass through the material and ionize the bulk material or impurities. The resulting electrons and holes are the source of energy for the voltaic but also may cause issues such as charge trapping at existing defect sites, which can change the resistivity, carrier lifetimes and diffusion lengths, and bandgap. [51] This damage tends to be temporary and is typically annealed to some degree over time with continuing radiation exposure.

Also of significance is nonionizing energy loss, particularly displacement damage where an atom is knocked out of its location in the material lattice to form a Frenkel defect pair of a vacancy and an interstitial atom. [51] Because these interstitial atoms are mobile, they may combine with other interstitials to form defect centers or combine with a vacancy to restore the lattice at that point. Over time during irradiation, equilibrium is reached in the creation and destruction of these defect centers. For highly ordered crystalline semiconductor devices, this displacement damage can change the properties enough to make the device fail.

6.2. Radiation Transport.

An alpha particle is a +2 charged helium ion resulting from the decay of a high atomic number radioactive nucleus while a beta particle is a high energy electron emitted when a neutron decays into a proton. When a charged particle moves through a material, its range is determined by the Bethe-Bloch equation:

$$-\frac{dE}{dx} = \frac{4\pi n z^2}{m_e v^2}\left(\frac{e^2}{4\pi\varepsilon_0}\right)^2\left[\ln\left(\frac{2m_e v^2}{I}\right)\right] \qquad \text{(Equation 6-1)}$$

where I is the material specific ionization potential. The U.S. National Institute of Standards and Technology (NIST) has a online calculator to determine the range of alpha particles in various materials. [52] For amorphous carbon (ρ=2.0g/cm^3), the range of a 5.48 MeV alpha particle from ^{241}Am is 4.96x10^{-3} g/cm^2. Dividing by the density results in a mean range for this alpha particle of ~ 25μm in amorphous carbon. A 500keV beta particle on the other hand has a range of ~125μm.

The ionization of the target material is not evenly distributed along the ion track as shown in Figure 6-1. As the ion slows down, the interaction cross-section between the material and the ion increases, resulting in a increased ionization rate. This has the practical implication that the number of electron hole pairs and defects is highest at the end of the ion track. Therefore, radioisotope voltaic devices should be designed to minimize the effect on device electronic and material properties due to these defect concentrations, particularly in the junction of a PN junction device.

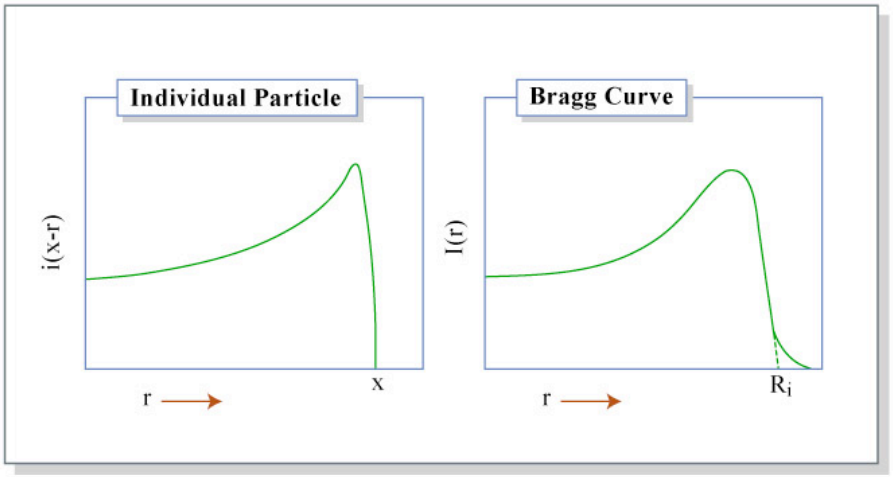

Figure 6-1 Bragg curve representing ionization in a target material due to a moving ion. The ion deposits most of energy near the end of the trail as represented by the peak. [53]

Previous work on alphavoltaics has shown that a PIN device has as much as 10 times the resistance to radiation degradation as a PN junction due to the much wider depletion region. [2] This larger depletion region allows the alpha particle deposition to occur outside the more critical active p- and n-type regions. Another option is to design the device such that the majority of the energy is lost in the substrate or contact material. While this will reduce the efficiency of the device, it will also reduce the degradation of the electronic properties of the junction.

6.3. Apparatus and Procedure

As there was insufficient time to run an adequate experiment to improve the PECVD PN junction and PIN device fabrication process, a more limited study to determine the impact alpha particle irradiation has on the Hall effect and Raman characteristics of individual doped and undoped films was undertaken. The

radiation source was a Isotope Products Lab ^{241}Am sealed source which emits alpha particles with an average energy of 5.5MeV at an activity of 42.26kBq (decays/sec). One each sulfur, boron, and undoped film was chosen with the goal of finding a previously characterized film the same size as or smaller then the window on the alpha particle source. A too large film would have an unirradiated portion that would impact the Hall effect measurements. The selected films are undoped a-C (2GPa), a-C:S(2.5%) 3GPa, and a-C:B(10%) 3GPa.

The films were irradiated to a fluence of 10^{10} alpha particles (5.5 days). After the irradiation time for a film was complete, the next film in the sequence began irradiation while the just removed film was immediately ran through the previously described Hall effect procedures. Each film was characterized immediately after irradiation. The goal was also to repeat the characterization after 5.5 days of isothermal room temperature annealing. The annealing characterization was to determine what, if any, recovery in electronic properties occurred after irradiation stopped.

6.4. Postirradiation Results

All three films were successfully characterized after irradiation, but only the sulfur doped film remained usable enough to be tested for annealing. The resistivity, mobility, and carrier concentration data are shown below in Figure 6-2. We recall there is a inverse relationship between mobility and both carrier concentration and resistivity.

Starting with the undoped film, we see that the resistivity postirradiation is essentially unchanged. The mobility increased by ~6X however while the carrier concentration decreased by ~6X. The Hall voltage indicated a shift to more strongly p-type. Mobility is inversely proportional to defect scattering, temperature dependent lattice scattering, and ionized impurity scattering. For mobility to increase, the amount of scattering must decrease. As temperature is roughly constant, there must be a reduced total of ionized impurity and defect scattering for the mobility to increase.

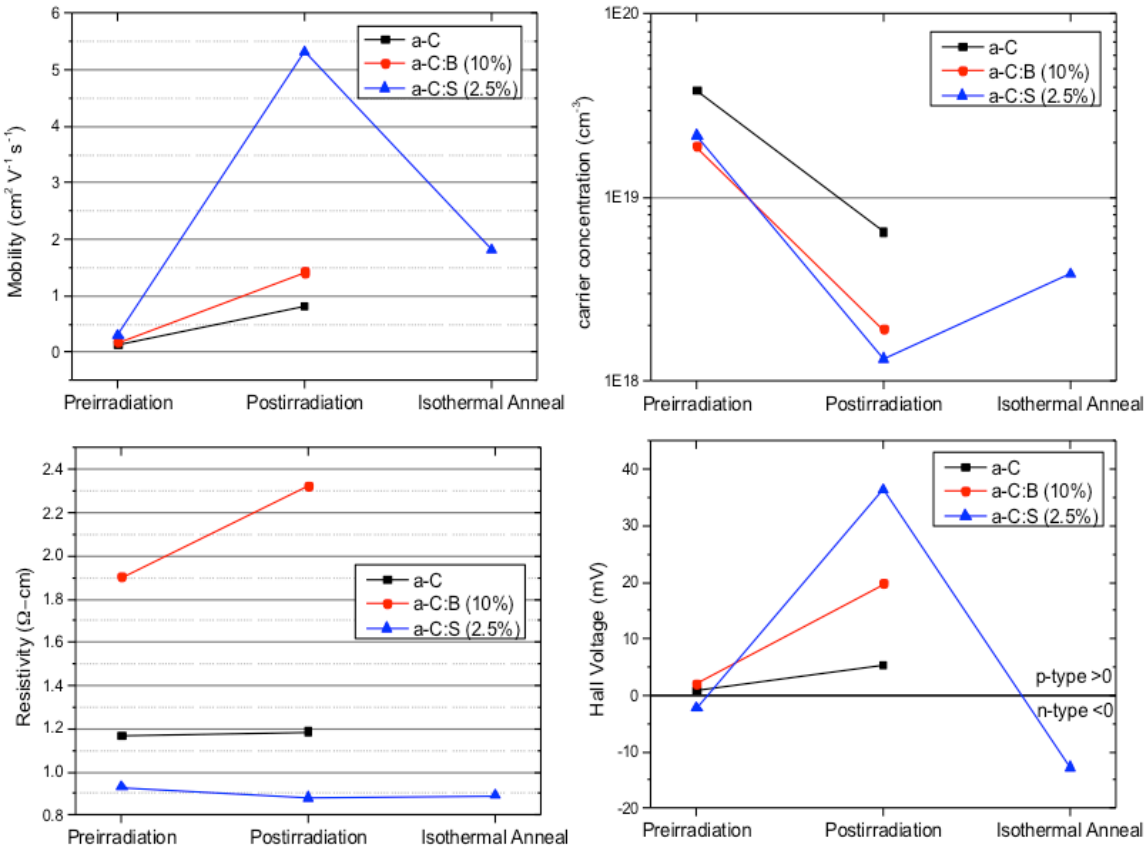

Figure 6-2. Postirradiation Hall effect data for undoped, sulfur, and boron doped films

From the undoped film postirradiation Raman results in Figure 6-3, we see that the G peak dispersion and I_D/I_G ratio decreased while the G peak width increased. This data indicates a general decrease in disorder and increase in sp^2 cluster size, both of which would act to reduce the defect scattering and increase mobility. While there is no Hall effect data available for isothermal annealing of the undoped films, the Raman data indicates that there is an overall trend of clustering and decreasing disorder after irradiation stops. This is likely due to the bond strain and disorder in the heavily damaged defect trails relaxing over time as recombination occurs and forms clusters of linked sp^2 rings.

For the boron-doped films, we see a resistivity increase of ~20%, a decrease in carrier concentration by an order of magnitude and an increase in mobility by ~8X while shifting to more strongly p-type. Similar to the undoped films, the decrease in I_D/I_G ratio and the G peak width indicate clustering, which would reduce scattering and increase mobility. The increase in G peak position would seem to contradict the clustering but the location at ~1588cm^{-1} is still less than that of the undoped films and therefore indicates a relative increase in clustering. The boron-doped films show the same pattern of clustering and decreasing disorder seen in the undoped films.

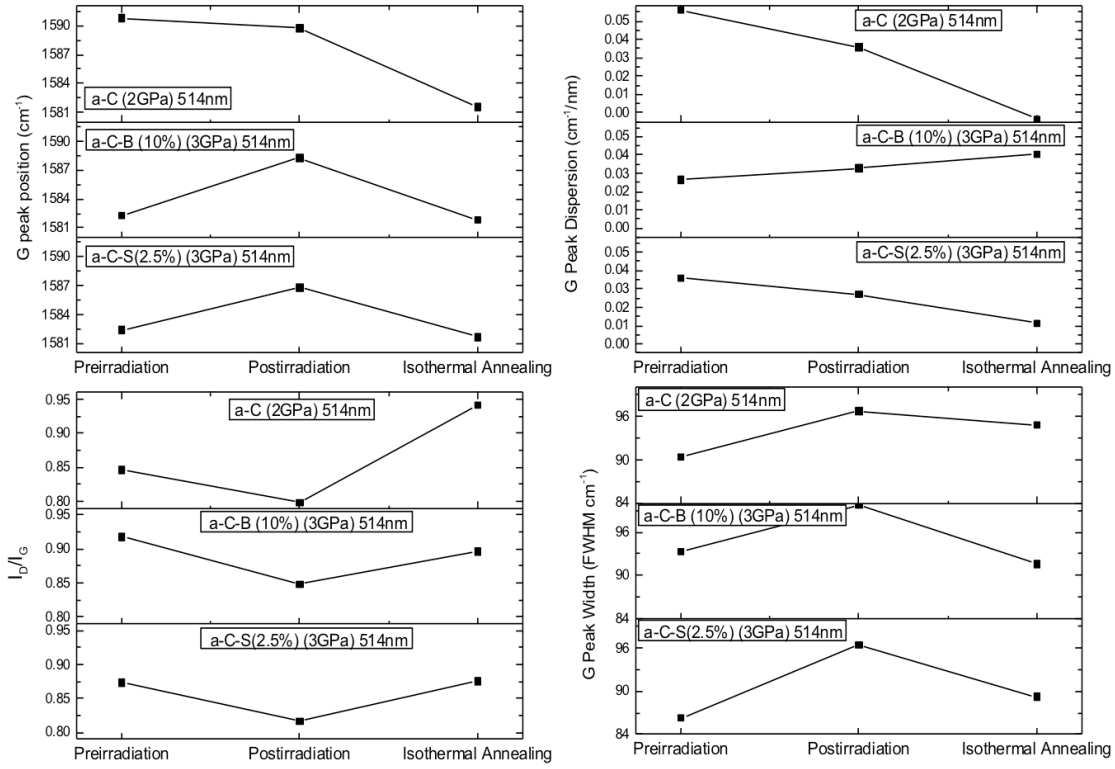

Figure 6-3. Raman results for the three irradiated films showing characteristics immediately following exposure to ~10^{10} alpha particles and then after 5.5 days isothermal room temperature anneal.

The sulfur-doped films were similar to the boron-doped films in that resistivity changed very little but the mobility and carrier concentration changes are even more dramatic. The mobility increased and the carrier concentration decreased by a factor of ~14X at the postirradiation measurement before recovering by a factor of three after isothermal annealing. Even after annealing, the mobility is still ~5X and carrier concentration ~1/5 the preirradiation values. The Hall voltage indicates a conversion from n-type to a relatively strong p-type immediately after irradiation but then conversion back to a more strongly n-type

material after annealing. The conversion to p-type is a common effect in n-type semiconductors due to both inactivation of the n-type dopants and introduction of defects that accept charge similarly to p-type dopants. Silicon may only recover 50% of the defects and may not revert to n-type without heating. [51] It appears the sulfur doped amorphous film is more resilient as it returns to n-type without thermal annealing. The Raman films show the same clustering pattern as both undoped and boron-doped films as they proceed from preirradiation to postirradiation then annealing.

7. Conclusions

The goals of this research were to investigate the doping of amorphous carbon nanopowders using thermomechanical processing and to fabricate relatively thick PN junction and PIN devices for use as radioisotope voltaic devices. If workable, this processing technique could develop thick films in a short time with low energy and material cost.

7.1. Undoped and Doped Carbon Films

The initial attempts to press undoped diamond and graphitized carbon black nanopowders met with little success as the films essentially remained in powder form even at temperatures of 250°C and 5GPa. A shift to an amorphous carbon nanopowder yielded much better results as the films were now coherent and robust enough tolerate manipulation during characterization. 3” stainless steel press plates

were needed to protect the hydraulic press platens while 0.25mm nickel substrates provided an adhesion-free surface for the films to be easily removed from.

Films pressed for 30 minutes were more stable than those pressed for lesser times and appeared as stable as films pressed for 60 minutes. A temperature of 109°C was utilized to avoid molten sulfur leaking out of the open sided pressing substrates. Both sulfur and boron carbide doped films were fabricated, characterized, and compared to undoped films.

The successful doping of n-type amorphous carbon films using sulfur has been demonstrated over a doping range of 2.5%, 5%, and 10% and 0.3-5GPa. Boron carbide (B_4C), using the same doping percentages, temperature and pressures, was found to be an inefficient dopant. In addition to acting as an n-type dopant, sulfur also significantly improved the stability of the carbon films. The undoped and boron doped films were much more brittle then sulfur doped films and broke easily during handling and characterization. Low power microscope images highlight parallel bands in the pressed films that likely indicate stresses in the films that lead to fracturing when handling.

Visible and near-infrared Raman spectroscopy indicates the doped and undoped films are almost entirely nanographitic sp^2 rings and display only slight changes in the bonding structure over the experiment temperature and pressures. For the undoped films, there is a slight increase in clustering and ring distortion as pressure increases. Higher temperatures and pressures may continue this process. Sulfur-doped films show a similar change in clustering with pressure that is

independent of doping percent. Boron-doped films on the other hand do not show the same degree of clustering as either the undoped or sulfur-doped films with pressure indicating the boron decreases the local ordering effect. There are no changes in the undoped or doped film Raman spectra that indicate significant conversion of sp^2 bonds to sp^3 at this pressure and temperature regime, which limits the ability to tailor the electronic properties of the films over a wider range.

The van der Pauw method was used to determine resistivity. The resistivity of undoped films was found to decrease nearly monotonically from 1.6Ω-cm to 1.2Ω-cm as pressure increased. Boron doped films behaved similarly at 0.3-1GPa pressures but then the resistivity increased as much as 70% above that of the undoped films from 2-5GPa. A second order polynomial surface model developed for boron-doped films indicates they are ~13X more sensitive to pressure then doping percent for P≥2GPa. Boron doping with boron carbide did not significantly change the film electronic properties and does not appear to be an effective dopant at these temperatures and pressures. Measuring the Hall voltage, both the undoped and doped films were found to be weakly p-type. Carrier concentrations for both undoped and doped films were similar at 1-6E19cm^{-3}. The average mobility of boron doped films increased to 0.211cm^2/V-s from 0.155cm^2/V-s although the standard deviations are large and overlap considerably. There was no clear trend in changes to mobility or carrier concentration with doping percent or pressure.

The resistivity of sulfur-doped films changed significantly from that of undoped films but appeared to be largely insensitive to pressure. The 2.5% and 10%

doped films resistivity decreased by a factor of two to ~0.6Ω-cm while the 5% doped films decreased by a factor of three to ~0.4Ω-cm. The sulfur-doped films fit a second order polynomial model well (adj R-square >0.986) which showed a ~5X greater sensitivity to doping percent than pressure. Most significantly, the Hall voltage showed sulfur-doped films converting to n-type. There is no clear change in carrier concentrations but average mobility increased from 0.155cm^2/V-s to 0.409cm^2/V-s suggesting an increase in ordering and decrease in defect scattering as also shown in the Raman results.

Irradiation and annealing studies using alpha particles was conducted and showed that undoped films became more slightly more p-type, boron-doped films more strongly p-type, and sulfur-doped films converting to the most strongly p-type. The sulfur-doped films converted back to more strongly n-type than preirradiation after isothermal annealing at 28°C for 5.5 days. The carrier concentration generally decreased by about an order of magnitude after irradiation for all film types. The mobility increased by 5-15X for all films after irradiation. The sulfur-doped film mobility did decrease after annealing but is still ~5X greater than preirradiation. Postirradiation and annealing Raman data indicated that there is an overall trend of clustering and decreasing disorder after irradiation stops. This is likely due to the bond strain and disorder in the heavily damaged defect trails relaxing over time as recombination occurs and forms clusters of linked sp^2 rings.

7.2. PN Junction and PIN Devices

PN junction and PIN devices were fabricated using two techniques. The first was to press individual undoped, boron-doped, and sulfur-doped films and then press them together into a device. The second technique was to use PECVD to deposit a p- or n-type boron carbide (or both) on a carbon film to form either a PN junction or PIN device. Despite using an experimental design that varied dopant percent and pressures for thermomechanical processing and a methodical one variable change during PECVD, no rectification was found in any of the PN or PIN devices regardless of fabrication technique. All measurable devices behaved similarly to resistors under I-V curve testing. The yield of usable films was much higher (6 of 9) using thermo-mechanical processing than with PECVD (2 of 13). PECVD is a highly energetic process that is proving challenging to use for fabricating carbon films as the majority of them were destroyed in the reactor chamber. Managing just substrate temperature and precursor temperature are likely insufficient to increase the film yield.

8. Recommendations for future research.

This research was a positive first step in the thermomechanical fabrication of relatively thick PN junction or PIN devices for use as alpha or beta voltaics. Future researchers could consider the following focus areas: optimizing the n-type doping using sulfur; evaluating whether boron is an effective p-type dopant; what processing parameters are required to convert sp^2 bonds to sp^3; parameters to

thermomechanically fabricate PN junctions and PIN devices; and exploration of radiation hardness and power output under irradiation.

To further explore both the n- and p-type doping and sp^2 to sp^3 conversion questions, I would considerably increase the available pressure and temperature options to push further into the diamond region of the carbon phase diagram and provide more energy to activate dopants. A hardened metal pressing system where two opposed 0.4cm diameter pistons fit inside a resistively heated cylinder would allow the 30-ton press to impart a maximum pressure of 20GPa. Resistive heating to ~800°C is reasonable with common lab equipment. I would create a fractional factorial design to fabricate doped films with these higher temperatures, pressures, and the original sulfur and B_4C precursors. Repeating the previous characterizations would allow comparison to earlier results.

If increasing the temperature and pressure range does not lead to an effective p–type dopant using B_4C, alternative dopants should be considered. Orthocarborane is known to dope p-type boron carbide after PECVD and could be compared to aluminum carbide in a fractional factorial design.

If issues still remain with brittleness despite increases in pressure, temperature or the above-mentioned alternative dopants, one option would be to consider polymers containing likely dopant atoms. Polymer crosslinking under high pressure, temperature, or UV irradiation is a common technique that may reduce the brittleness of the films.

In addition to repeating the previous characterization techniques, it would be useful to conduct Raman spectroscopy using a 244nm laser to excite the σ-σ* transitions. This would allow direct observation of the sp^3 bonding in the film vice inferring sp^3 content from the sp^2 changes seen in visible-NIR Raman. In addition to UV Raman, I would also conduct studies using UV-VIS-NIR spectroscopy or ellipsometry to assess impact on bandgap due to variable processing parameters.

The next challenge will be to develop the relatively abrupt junctions that are critical to PN junction and PIN device performance. The pressing cylinder and piston set would be helpful to contain the film edges, leave a smoother surface, and allow increased pressure without film damage. I-V curve characterization to assess rectification is critical to ultimately developing functional voltaic devices.

Once serviceable devices are fabricated, ionized radiation sources and light sources would be used along with I-V curve measurements to determine power output characteristics and compared to common photovoltaic devices using metrics such as fill factor, open circuit voltage, short circuit current, and efficiency. Radiation hardness would be assessed by monitoring power output over time to determine the extent of any degradation as a function of fluence. An experiment to evaluate impact of short heating cycles, with a range of 1-30 minutes at temperatures of 28-200°C, on power output would be invaluable to assess ways to lengthen the lifetime of the devices.

References.

[1] J. P. Fleurial, G. J. Snyder, J. Patel, J. A. Herman, T. Caillat, B. Nesmith*, et al.*, "Miniaturized radioisotope solid state power sources," *AIP Conference Proceedings,* vol. 504, p. 1500, 2000.

[2] C. D. Cress, B. J. Landi, R. P. Raffaelle, and D. M. Wilt, "InGaP alpha voltaic batteries: Synthesis, modeling, and radiation tolerance," *Journal of Applied Physics,* vol. 100, p. 114519, 2006.

[3] F. J.-P, R. M.A, S. G.J, H. C.-K, W. J.F, P. J*, et al.*, "Micro/Nano Fabricated Solid-State Thermoelectric Generator Devices for Integrated High Voltage Power Sources," in *IAF abstracts, 34th COSPAR Scientific Assembly*.

[4] T. Wacharasindhu, J. W. Kwon, D. E. Meier, and J. D. Robertson, "Radioisotope microbattery based on liquid semiconductor," *Applied Physics Letters,* vol. 95, pp. 014103-014103, 2009.

[5] J. N. Harb, R. M. LaFollette, R. H. Selfridge, and L. L. Howell, "Microbatteries for self-sustained hybrid micropower supplies," *Journal of Power Sources,* vol. 104, pp. 46-51, Jan 2002.

[6] S. G. Bailey, D. M. Wilt, S. L. Castro, C. D. Cress, and R. P. Raffaelle, "Photovoltaic development for alpha voltaic batteries," *Photovoltaic Specialists Conference, 2005,* pp. 106-109, 2005.

[7] C. D. Cress, B. J. Landi, and R. P. Raffaelle, "Modeling laterally-contacted nipi-diode radioisotope batteries," *IEEE Transactions on Nuclear Science,* vol. 55, pp. 1736-1743, 2008.

[8] R. P. Raffaelle, P. Jenkins, D. Wilt, D. Scheiman, D. Chubb, and S. Castro, "Alpha voltaic batteries and methods thereof," 2010.

[9] G. J. Snyder, J. Patel, and J.-P. Fleurial, "Extremely-efficient, miniaturized, long-lived alpha-voltaic power source using liquid gallium," 2004.

[10] K. S. Liao, S. D. Yambem, A. Haldar, N. J. Alley, and S. A. Curran, "Designs and Architectures for the Next Generation of Organic Solar Cells," *Energies,* vol. 3, pp. 1212-1250, Jun 2010.

[11] S. m. Sze, *Semiconductor Devices - Physics and Technology*, 1st ed. vol. 1: John Wiley & Sons, 1985.

[12] A. C. Mayer, S. R. Scully, B. E. Hardin, M. W. Rowell, and M. D. McGehee, "Polymer-based solar cells," *Materials Today,* vol. 10, pp. 28-33, 2007.

[13] H. W. Zhu, J. Q. Wei, K. L. Wang, and D. H. Wu, "Applications of carbon materials in photovoltaic solar cells," *Solar Energy Materials and Solar Cells,* vol. 93, pp. 1461-1470, Sep 2009.

[14] F. P. Bundy, W. A. Basset, M. S. Weathers, R. J. Hemley, H. K. Mao, and A. F. Goncharov, "The pressure-temperature phase and transformation diagram for carbon; updated through 1994," *Carbon,* vol. 34, pp. 141-53, 1996.

[15] J. Robertson, "Diamond-like amorphous carbon," *Materials Science and Engineering: R: Reports,* vol. 37, pp. 129-281, 2002.

[16] C. Casiraghi, J. Robertson, and A. C. Ferrari, "Diamond-like carbon for data and beer storage," *Mater. Today (Oxford, U. K.),* vol. 10, pp. 44-53, 2007.

[17] J. Robertson, "Improving the properties of diamond-like carbon," *Diamond Relat. Mater.,* vol. 12, pp. 79-84, 2003.

[18] A. Ilie, O. Harel, N. M. J. Conway, T. Yagi, J. Robertson, and W. I. Milne, "Photoconductivity of nitrogen-modified hydrogenated tetrahedral amorphous carbon," *Journal of Applied Physics,* vol. 87, pp. 789-794, 2000.

[19] F. Alibart, O. D. Drouhin, M. Benlahsen, S. Muhl, S. E. Rodil, E. Camps*, et al.*, "Comparison and semiconductor properties of nitrogen doped carbon thin films grown by different techniques," *Applied Surface Science,* vol. 254, pp. 5564-5568, Jun 2008.

[20] M. Guerino, A. P. Mousinho, M. Massi, and R. D. Mansano, "Electrical Conduction Mechanisms of Nitrogenated Amorphous Carbon Films Deposited by High-Density Plasma Chemical Vapor Deposition," *Plasma Processes and Polymers,* vol. 2, pp. 454-457, 2005.

[21] N. E. Derradji, M. L. Mahdjoubi, H. Belkhir, N. Mumumbila, B. Angleraud, and P. Y. Tessier, "Nitrogen effect on the electrical properties of CNx thin films deposited by reactive magnetron sputtering," *Thin Solid Films,* vol. 482, pp. 258-263, 2005.

[22] C. Arena, B. Kleinsorge, J. Robertson, W. I. Milne, and M. E. Welland, "Electronic properties of tetrahedral amorphous carbon investigated by scanning tunneling microscopy," *Journal of Applied Physics,* vol. 85, pp. 1609-1615, 1999.

[23] V. S. Veerasamy and et al., "n-type doping of highly tetrahedral diamond-like amorphous carbon," *Journal of Physics: Condensed Matter,* vol. 5, p. L169, 1993.

[24] L. Kumari and S. V. Subramanyam, "Structural, optical and electrical properties of sulfur-incorporated amorphous carbon films," *Applied Physics A: Materials Science & Processing,* vol. 95, pp. 343-349, 2009.

[25] S. Gupta, B. R. Weiner, and G. Morell, "Electronic structure of sulfur-modified nanocrystalline carbon films," *Journal of Applied Physics,* vol. 97, pp. 094307-6, 2005.

[26] Z. Q. Ma and B. X. Liu, "Boron-doped diamond-like amorphous carbon as photovoltaic films in solar cell," *Solar Energy Materials and Solar Cells,* vol. 69, pp. 339-344, Nov 2001.

[27] M. Ma, Q. Xue, H. Chen, X. Zhou, D. Xia, C. Lv*, et al.*, "Photovoltaic characteristics of Pd doped amorphous carbon film/SiO2/Si," *Appl. Phys. Lett.,* vol. 97, pp. 061902/1-061902/3, 2010.

[28] D. S. Zhao, M. Zhao, and Q. Jiang, "Size and temperature dependence of nanodiamond-nanographite transition related with surface stress," *Diamond Relat. Mater.,* vol. 11, pp. 234-236, 2002.

[29] M. A. Baklar, F. Koch, A. Kumar, E. B. Domingo, M. Campoy-Quiles, K. Feldman*, et al.*, "Solid-State Processing of Organic Semiconductors," *Adv. Mater. (Weinheim, Ger.),* vol. 22, pp. 3942-3947, 2010.

[30] H. S. Nalwa, Ed., *Nanostructured Materials and Technology*. San Diego, CA: Academic Press, 2002, p.^pp. Pages.

[31] Wikipedia. (2012, 7 August). *Sulfur*. Available: http://en.wikipedia.org/wiki/Sulfur

[32] Wikipedia. (2012, 7 August). *Boron Carbide*. Available: http://en.wikipedia.org/wiki/Boron_carbide

[33] H. Akasaka, T. Imai, and N. Ohtake, "Fabrication and properties of a-C:H/boron-doped diamond structure," *New Diamond Front. Carbon Technol.,* vol. 17, pp. 301-308, 2007.

[34] B. Kleinsorge, A. Ilie, M. Chhowalla, W. Fukarek, W. I. Milne, and J. Robertson, "Electrical and optical properties of boronated tetrahedrally bonded amorphous carbon (ta-C:B)," *Diamond Relat. Mater.,* vol. 7, pp. 472-476, 1998.

[35] S. Ohmagari, T. Yoshitake, A. Nagano, R. Ohtani, H. Setoyama, E. Kobayashi*, et al.*, "Formation of p-type semiconducting ultrananocrystalline diamond/hydrogenated amorphous carbon composite films by boron doping," *Jpn. J. Appl. Phys.,* vol. 49, pp. 031302/1-031302/4, 2010.

[36] O. S. Panwar, M. A. Khan, B. S. Satyanarayana, S. Kumar, and Ishpal, "Properties of boron and phosphorous incorporated tetrahedral amorphous carbon films grown using filtered cathodic vacuum arc process," *Appl. Surf. Sci.,* vol. 256, pp. 4383-4390, 2010.

[37] P. K. Sitch, T. Koehler, G. Jungnickel, D. Porezag, and T. Frauenheim, "A theoretical study of boron and nitrogen doping in tetrahedral amorphous carbon," *Solid State Commun.,* vol. 100, pp. 549-553, 1996.

[38] M. Tan, J. Zhu, J. Han, W. Gao, A. Liu, and X. Han, "Raman characterization of boron doped tetrahedral amorphous carbon films," *Mater. Res. Bull.,* vol. 43, pp. 453-462, 2008.

[39] P. N. Vishwakarma and S. V. Subramanyam, "Metal-insulator transition in boron-doped amorphous carbon films," *Philos. Mag.,* vol. 87, pp. 811-821, 2007.

[40] C. H. Choi, S. H. Park, and S. I. Woo, "Heteroatom doped carbons prepared by the pyrolysis of bio-derived amino acids as highly active catalysts for oxygen electro-reduction reactions," *Green Chem.,* vol. 13, pp. 406-412, 2011.

[41] S. Glenis, A. J. Nelson, and M. M. Labes, "Sulfur doped graphite prepared via arc discharge of carbon rods in the presence of thiophenes," *J. Appl. Phys.,* vol. 86, pp. 4464-4466, 1999.

[42] S. Gupta, B. R. Weiner, and G. Morell, "Ex situ spectroscopic ellipsometry and Raman spectroscopy investigations of chemical vapor deposited sulfur incorporated nanocrystalline carbon thin films," *Journal of Applied Physics,* vol. 92, p. 5457, 2002.

[43] E. Z. Kurmaev, A. V. Galakhov, A. Moewes, S. Moehlecke, and Y. Kopelevich, "Interlayer conduction band states in graphite-sulfur composites," *Physical Review B,* vol. 66, p. 193402, 2002.

[44] I. Sakaguchi, M. N.-Gamo, Y. Kikuchi, E. Yasu, H. Haneda, T. Suzuki*, et al.*, "Sulfur: A donor dopant for n-type diamond semiconductors," *Physical Review B,* vol. 60, p. R2139, 1999.

[45] A. C. Ferrari and J. Robertson, "Interpretation of Raman spectra of disordered and amorphous carbon," *Physical Review B,* vol. 61, p. 14095, 2000.

[46] A. C. Ferrari and J. Robertson, "Raman spectroscopy of amorphous, nanostructured, diamond-like carbon, and nanodiamond," *Philos. Trans. R. Soc. London, Ser. A,* vol. 362, pp. 2477-2512, 2004.

[47] N. US Department of Commerce. (2012). *The Hall Effect*. Available: http://www.nist.gov/pml/div683/hall_effect.cfm - vanderpauw

[48] R. Langley, *Practical statistics simply explained*, Rev. ed. New York,: Dover Publications, 1971.

[49] J. Singh. (17 June). *SEMICONDUCTOR DEVICES: BASIC PRINCIPLES*. Available: http://www.eecs.umich.edu/~singh/semi.html

[50] S. Instruments. (17 June). Available: http://www.imagesco.com/articles/photovoltaic/photovoltaic-pg4.html

[51] A. Holmes-Siedle and L. Adams, *Handbook of Radiation Effects, 2nd Edition*: Oxford University Press, 2002.

[52] NIST. *Alpha Particle Stopping Power*. Available: http://physics.nist.gov/PhysRefData/Star/Text/ASTAR.html

[53] M. OpenCourseware. (2006, 21 June). *Applied Nuclear Physics*. Available: http://www.flickr.com/photos/mitopencourseware/3775447720/in/set-72157621892931990

Appendix A van der Pauw Worksheet

Van der Pauw Hall Measurement Worksheet

Sample Identification _____
Thickness if known (cm) _____ Dimensions _____
Date _____ Lab _____ Operator _____
Chemical Pretreatment (if any) _____
Contact Metal _____ Contact Process _____
Comments _____

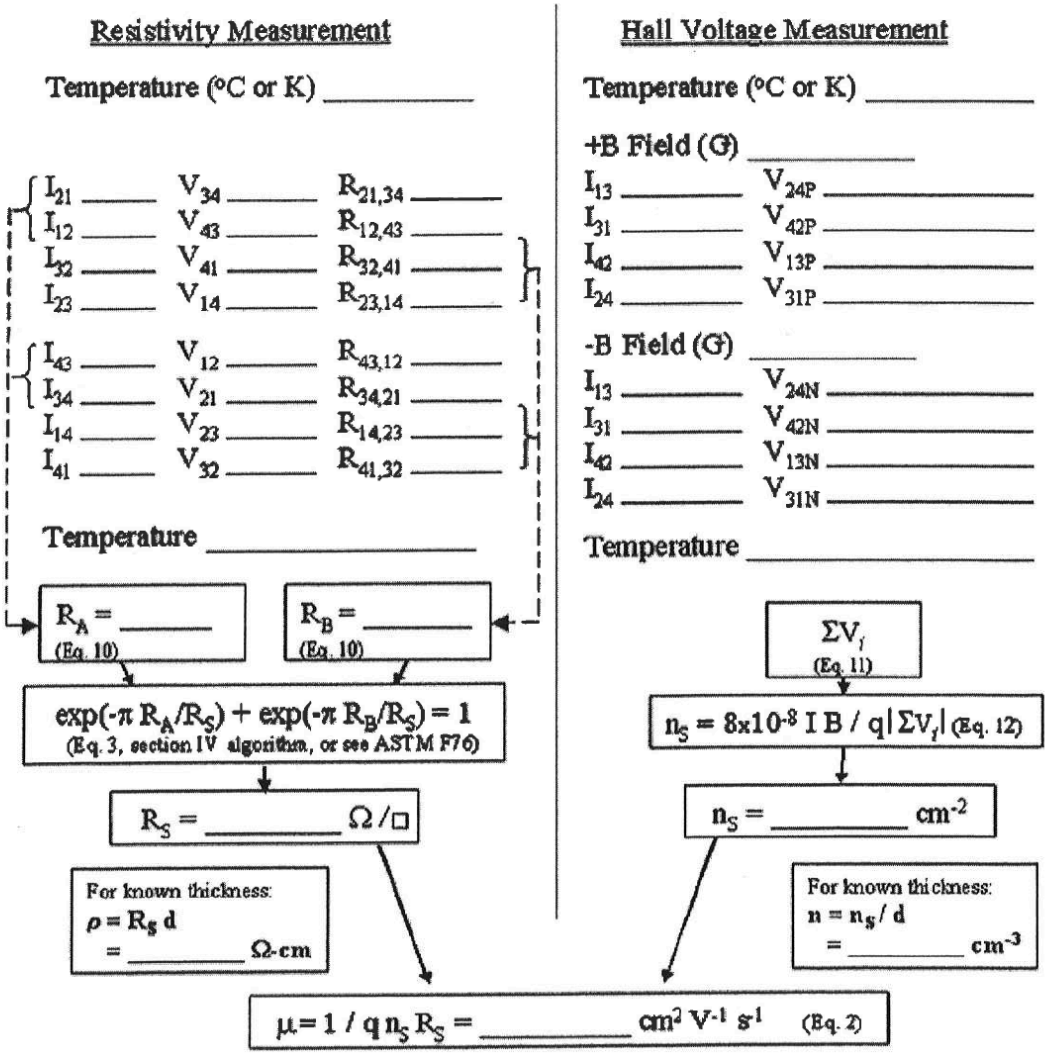

Appendix B Wilcoxon Sign Test

The Wilcoxon Signed Ranks Test is used to compare two matched samples and determine whether there is a significant difference between the two paired measurements. The principle behind this test is not only that it takes into account the direction of differences but the magnitude as well. The signed ranks test example in Table B-1 below is based on a comparison of the resistivity of a-C compared to a-C:B(5%) over the range of 0.3-5.0GPa.

Table B-1. Example Wilcoxon Signed Ranks Test.

Ordered Difference Value $[\rho_{a\text{-}C} - \rho_{a\text{-}C:B(5\%)}]$	Tally	Rank Values	+ Ranks	- Ranks
0.007	+	1	1	
0.069	+	2	2	
0.089	-	3		3
0.321	-	4		4
0.461	-	5		5
0.788	-	6		6
Rank Total:			3	18
Smaller Rank Total = 3				

Using Origin software to calculate the z value results in a >90% (92.2%) probability that these two samples are significantly different. In this example, even though 2 of the a-C films have a greater resistivity than the matched a-C:B(5%) films, they have considerably smaller difference values (0.007, 0.069) and doesn't detract from a high probability that the films are different.

Appendix C Detailed PECVD Procedure

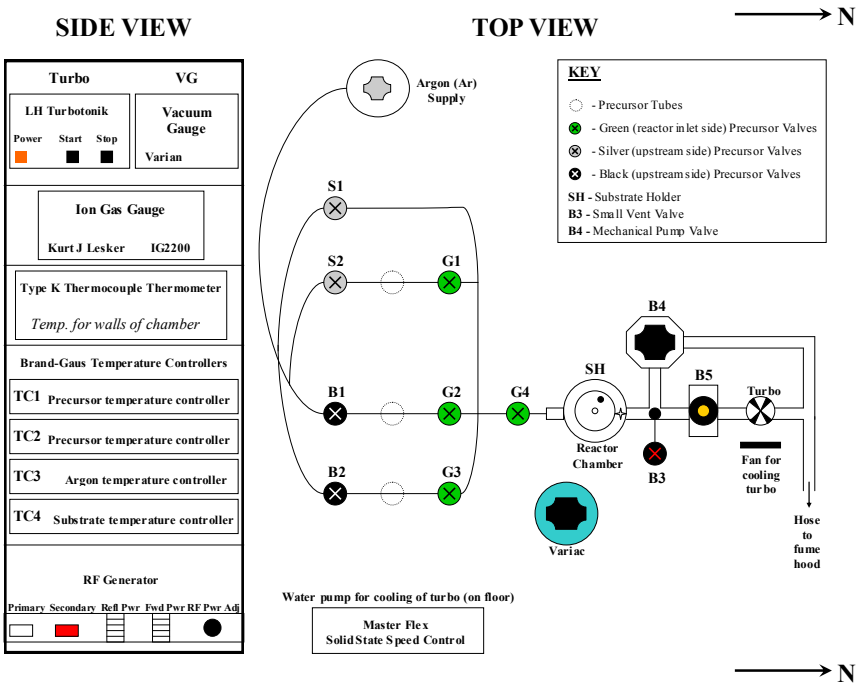

Figure C-1. Schematic of the plasma enhanced chemical vapor deposition (PECVD) system.

a. The normal configuration for the reactor when not in use is under vacuum such that valve (B4) is open and all other valves are closed. To bake out overnight, heat the argon supply line (TC3) to 102°C to bake out and heat the reactor walls to 102°C (~75 on the Variac). Argon tank valve should be closed and valves (S1) and (G4) open.

b. Turn on the RF primary power at least 15 minutes prior to creating a plasma so that the system is warmed up. Prepare Ni substrates by cutting to 1.5cm X 1.5cm and ultrasonic cleaning in acetone then ethanol for 10 minutes each.

c. To remove the substrate holder, close all valves and slowly open valve (B3). Monitor the vacuum gauge (VG); when gauge goes to “ATM”, the substrate holder can be removed.

d. Once the substrates are ready, clean the substrate holder, mask, and screws with Kimwipes and acetone/ethanol. Ultrasonic cleaning of the mask in ethanol or acetone may also be done. Dry all parts with the helium gun.

e. Using clean tools and clean gloves, place the substrates on the substrate holder and tighten the mask with clean nuts and bolts. Tighten screws in a clockwise fashion to avoid warping of the mask.

f. Insert the substrate holder into the reactor’s chamber and ensure the O-ring is not pinched. Orient the substrate holder so that the screw on top is pointing to the “north” in order to monitor growth rates as film thicknesses will vary. Install the cartridge heater and the thermocouple into the substrate holder.

g. Verify valve (B3) is closed and open (S1) and (G4). Allow vacuum pressure to fall as far as the mechanical pump (B4) will go.

h. Turn on argon temperature controller (TC3) to 60^{o}C.

i. Activate the turbo pump by pushing the “Start” button on the LH Turbotronik controller and turn on the accessory cooling fan. When the “NORM” light on the LH Turbotronik controller comes on, close the mechanical pump valve (B4) and open the turbo valve (B5).

j. Turn on the substrate temperature controller (TC4) and set to 150°C for carbon substrates. To do this, on (TC4) press the “right” arrow key then press the

“up” arrow key to adjust to desired temperature. To set the temperature, press the “right” arrow key.

k. After 10 minutes of pumping with the substrate up to the desired temperature, turn off the turbo by pushing “Stop” on the LH Turbotronik controller. Open the mechanical pump valve (B4) and close the turbo valve (B5).

l. Open the argon tank valves and set the pressure to about 200 mTorr by slowly opening and adjusting valve (S1). Continue purging for a minute or two after which the plasma should be struck by turning on the RF secondary power and setting the power adjustment knob to ~25W.

m. Begin heating precursors to desired temperature (45°C metacarborane, 70°C orthocarborane) to ensure vaporization is at a maximum before deposition.

n. Plasma etch for 10 minutes. After etching, stop the plasma and decrease the argon pressure to 150 mTorr.

o. With the plasma off, open the desired carborane precursor valves and regulate to 225mTorr by adding to the argon base pressure. Once stabilized, restrike the plasma as discussed above and grow film for desired time.

p. NOTE: Always open precursor valves from right to left (e.g. G1 then S2) and close valves from left to right (e.g. B1 then G2) to minimize pressure spikes in the reactor.

q. To terminate the deposition process, close the precursor valves. Turn the RF power adjustment knob counterclockwise until it stops and switch off the RF power secondary switch. Flush with argon again using ~2000mTorr to help remove

un-decomposed precursors. Let the RF generator run for at least 15 minutes before the RF primary power is switched off to allow proper cool down of the RF generator.

r. Close the Ar valves (S1 and tank valve) and the reactor's inlet valve (G4).

s. Switch off all temperature controllers and heaters.

t. If additional deposition required on other film, allow film to cool to room temperature before removing, flipping over and repeating the above deposition procedures.